JGR Oceans

RESEARCH ARTICLE
10.1029/2020JC017091

Physical Controls on the Macrofaunal Benthic Biomass in Barrow Canyon, Chukchi Sea

Robert S. Pickart[1], Michael A. Spall[1], Peigen Lin[1], Frank Bahr[1], Leah T. McRaven[1], Kevin R. Arrigo[2], and Jacqueline M. Grebmeier[3]

[1]Department of Physical Oceanography, Woods Hole Oceanographic Institution, Woods Hole, MA, USA, [2]Department of Earth System Science, Stanford University, Stanford, CA, USA, [3]University of Maryland Center for Environmental Science, Solomons, MD, USA

Key Points:

- Shipboard transects across Barrow Canyon reveal vertical plumes of fluorescence and oxygen extending to the bottom when the flow is strong
- Solution of the quasi-geostrophic omega equation reveals that downwelling on the cyclonic side of the current drives the plumes
- This source of carbon to the seafloor can explain the enhanced levels of macrofaunal benthic biomass in the center of Barrow Canyon

Correspondence to
R. S. Pickart,
rpickart@whoi.edu

Citation:
Pickart, R. S., Spall, M. A., Lin, P., Bahr, F., McRaven, L. T., Arrigo, K. R., & Grebmeier, J. M. (2021). Physical controls on the macrofaunal benthic biomass in Barrow Canyon, Chukchi Sea. *Journal of Geophysical Research: Oceans*, *126*, e2020JC017091. https://doi.org/10.1029/2020JC017091

Received 16 DEC 2020
Accepted 12 APR 2021

Abstract A region of exceptionally high macrofaunal benthic biomass exists in Barrow Canyon, implying a carbon export process that is locally concentrated. Here we offer an explanation for this benthic "hotspot" using shipboard data together with a set of dynamical equations. Repeat occupations of the Distributed Biological Observatory transect in Barrow Canyon reveal that when the northward flow is strong and the density front in the canyon is sharp, plumes of fluorescence and oxygen extend from the pycnocline to the seafloor in the vicinity of the hotspot. By solving the quasi-geostrophic omega equation with an analytical flow field fashioned after the observations, we diagnose the vertical velocity in the canyon. This reveals that, as the along stream flow converges into the canyon, it drives a secondary circulation cell with strong downwelling on the cyclonic side of the northward flow. The downwelling quickly advects material from the pycnocline to the seafloor in a vertical plume analogous to those seen in the observations. The plume occurs only when the phytoplankton reside in the pycnocline, since the near-surface vertical velocity is weak, also consistent with the observations. Using a wind-based proxy to represent the strength of the northward flow and hence the pumping, in conjunction with a satellite-derived phytoplankton source function, we construct a time series of carbon supply to the bottom of Barrow Canyon.

Plain Language Summary In this study, we use shipboard occupations of a transect across Barrow Canyon in the northeast Chukchi Sea, together with a set of dynamical equations, to explain why exceptionally large concentrations of macrofauna are found on the seafloor there. The observations reveal that when the northward flow through the canyon is strong and a sharp cross-canyon density contrast is present, plumes of phytoplankton extend from the middle of the water column to the seafloor in the vicinity of this benthic "hotspot." Using an idealized representation of the canyon flow, we solve the equations for the vertical velocity. This reveals that, as the northward flow accelerates through the canyon, strong downward velocities quickly transfer the phytoplankton to the bottom—in line with the observations. Since the strength of the current depends on the wind, we develop a proxy for the pumping using a nearby wind record. Using satellite data, we also construct a record of the amount of phytoplankton entering the canyon. Together, this provides an estimate of the food supply to the bottom of Barrow Canyon.

1. Introduction

The Chukchi Sea is one of the most productive regions of the Arctic Ocean (Springer & McRoy, 1993), in part because of the high levels of nutrients advected through the Bering Strait (Grebmeier, Bluhm, et al., 2015). Furthermore, due to the recent decline in sea ice cover and higher percentage of thin first-year ice, light levels have increased which has led to even larger levels of annual production (Arrigo & van Dijken, 2011). Since the Chukchi shelf is an export-dominated regime, the large amount of carbon that reaches the seafloor supports robust levels of benthic activity (Grebmeier, Bluhm, et al., 2015). This in turn influences benthic-feeding higher trophic species such as walrus, whales, and sea birds (Grebmeier, Cooper, et al., 2006).

The levels of benthic macrofaunal biomass vary regionally across the Chukchi shelf, with several well-defined "hot spots" (Figure 1). The broad area of enhanced biomass northwest of Bering Strait is associated with particularly high levels of nitrate that are advected into the region with the Anadyr water (Fang

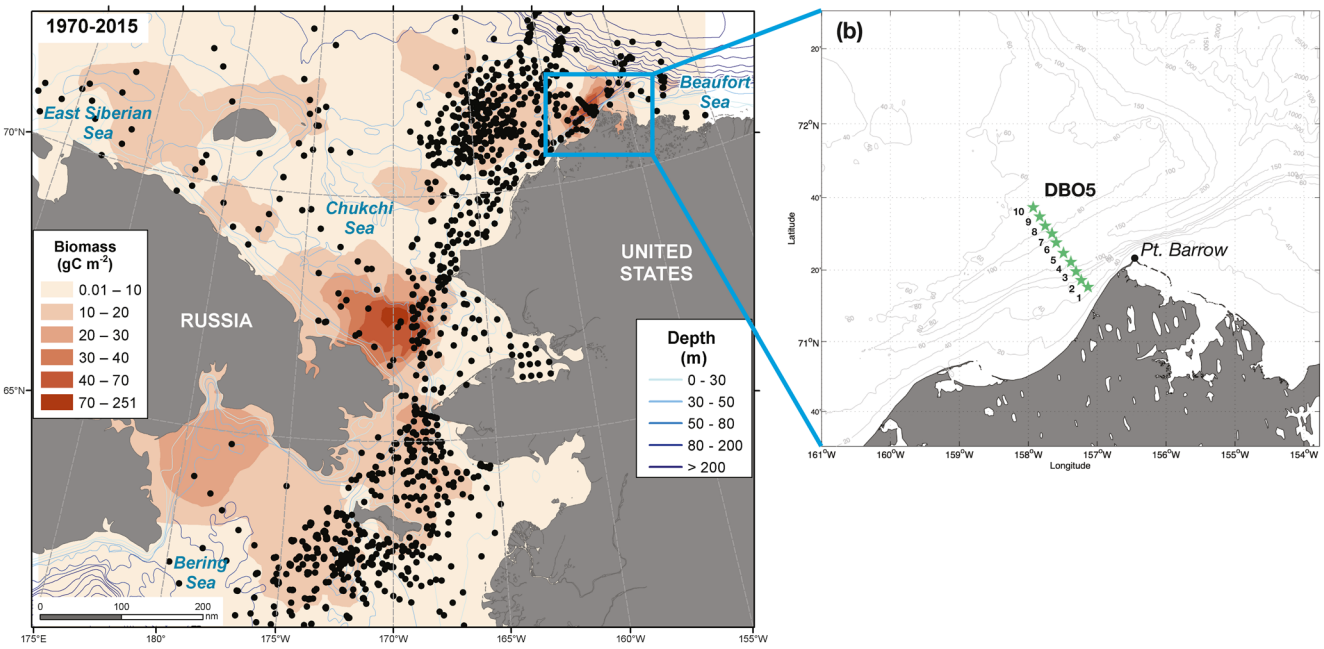

Figure 1. (a) Lateral distribution of macrofaunal benthic biomass in the northern Bering and Chukchi Seas using measurements from 1999 to 2015 (updated from Grebmeier, Cooper, et al., 2006). (b) The 10 CTD stations comprising Distributed Biological Observatory transect #5 (DBO5). The station numbers increase with offshore distance. The bathymetry is from IBCAO v3.

et al., 2020). This spurs enhanced primary production, and the lack of sufficient zooplankton grazers in summer leads to a greater food supply for the macrobenthic fauna. In the northeast Chukchi Sea, the region southeast of Hanna Shoal is also characterized by elevated levels of macrofaunal benthic biomass (though not as pronounced as farther south; Figure 1). It has been demonstrated that the circulation in this region pools nutrients late in the season (Lin, Pickart, McRaven, et al., 2019), which is conducive for fall blooms. This would result in a more continuous supply of carbon to the benthos throughout the open water season.

Barrow Canyon, which cuts into the northeastern-most part of the Chukchi shelf, is another location where elevated levels of benthic biomass are persistently measured (Grebmeier, Bluhm, et al., 2015). Unlike the above-described regions, however, this hotspot is quite geographically confined: the biomass is greatest in the deepest part of the canyon (Figure 2), centered mid-way along its length. A decades-long time series of macrofaunal biomass has shown that this is a persistent feature (Grebmeier, Bluhm, et al., 2015). Also,

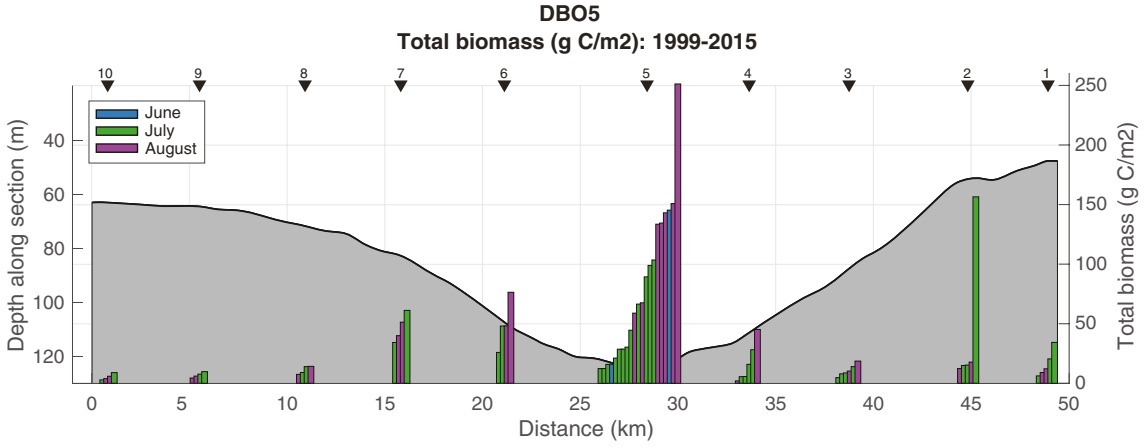

Figure 2. Distribution of benthic biomass across the DBO5 line using data from 1999 to 2015, delineated by month. The station positions/names are marked along the top. The bathymetry is from *Healy*'s echosounder. See Grebmeier and Cooper (2020) for methods and cruise information.

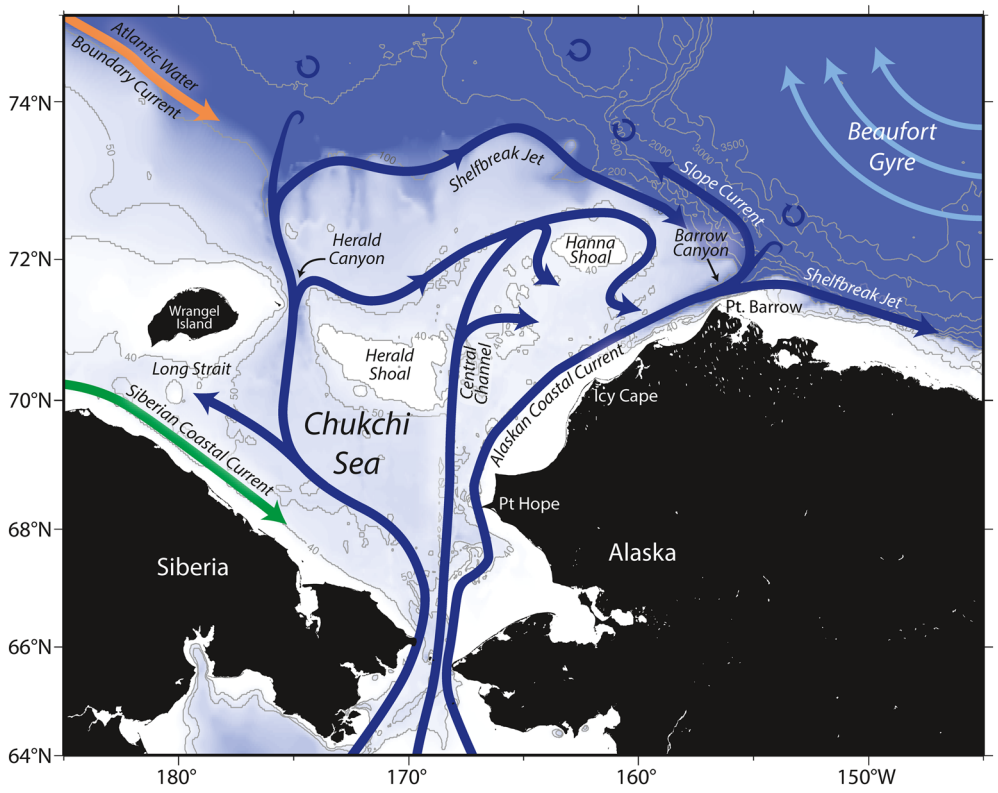

Figure 3. Schematic circulation of the Chukchi Sea and place names, after Corlett and Pickart (2017).

unlike the other two regions, the flow through the canyon is quite strong throughout summer and fall. Using three-dimensional particle tracking in a numerical model, Feng et al. (2021) concluded that, for carbon settling rates on the order of meters per day, the surface source of food for macrofauna in Barrow Canyon would be located hundreds of kilometers upstream (to the south). On the other hand, enhanced turbulent mixing in the canyon (Beaird et al., 2020; Shroyer, 2012) could lead to an upward flux of nutrients from the sea floor that in turn might support local primary production. However, this does not explain the fact that the hotspot is confined to such a limited region within the canyon, especially in light of the strong flow.

Barrow Canyon is a critical choke point of the circulation on the Chukchi shelf (Figure 3). The coastal pathway—known as the Alaskan Coastal Current (ACC) in the summer months—flows directly from Bering Strait to Barrow Canyon (Paquette & Bourke, 1974). Additionally, the central shelf pathway ultimately drains into the canyon via different routes (Pickart, Moore, et al., 2016; Weingartner, Aagaard, et al., 2005; Figure 3), as does a portion of the western pathway (Pickart, Moore, et al., 2016). Averaged over the year, the transport through the mouth of the canyon is estimated to be 0.44 ± 0.07 Sv (Itoh, Nishino, et al., 2013), which is nearly half of the annual mean transport of Pacific Water through Bering Strait (1.0 ± 0.5 Sv; Woodgate, 2018). However, during the warm months of the year, the volume transport in the canyon can exceed 1 Sv (Gong & Pickart 2015; Itoh, Pickart, et al., 2015). Due to the constricted topography of the canyon, the flow accelerates as it drains northward toward the basin (Lin, Pickart, McRaven, et al., 2019; Pisareva, Pickart, Spall, et al., 2015). When the ACC is present, the canyon velocities can be on the order of 1 m s^{-1} (Itoh, Pickart, et al., 2015).

Through the course of the year, different Pacific-origin water masses are advected through Barrow Canyon. From December to May the predominant water mass is Newly Ventilated Winter Water (Pisareva, Pickart, Lin, et al., 2019), which is very cold (near the freezing point) and high in nutrients (Arrigo et al., 2017; Pacini et al., 2019; Pickart, Moore, et al., 2016). As the season progresses, this water mass warms through mixing and solar heating on the shelf (Gong & Pickart 2016) and is termed Remnant Winter Water, which can still have moderate concentrations of nitrate. From mid-summer to fall, warm and fresh Alaskan Coastal Water

Table 1
Occupations of the DBO5 Transect Considered in the Study

Cruise ID	Date	Elapsed time of occupation	Pumping	Non-pumping	Plumes	Upwelling	% strong NE wind
HLY0904	6 Aug 2009	7.0 hrs	X		X		5.5
HLY1003	7 Sep 2010	7.3 hrs	X		X		5.6
HLY1101	22 Jul 2011	15.2 hrs	X		X		2.8
HLY1103	7 Oct 2011	7.0 hrs		X			47.2
HLY1303	12 Oct 2013	6.8 hrs		X			37.5
HLY1303	24 Oct 2013	6.6 hrs	X				2.8
HLY1402*	15 Jul 2014	8.5 hrs	X		X		0
HLY1702*	1 Sep 2017	19.6 hrs				X	73.6
HLY1801	17 Aug 2018	16.3 hrs		X			11.1
HLY1803*	14 Nov 2018	9.5 hrs				X	9.7
HLY1901	6 Aug 2019	15.9 hrs	X		X		0

* Not considered in the study.

Notes. The pumping cases are highlighted light red; the nonpumping cases are highlighted light blue. The three realizations not considered in the study are marked with an asterisk and not highlighted (see text).

is transported by the ACC through the eastern side of the canyon, as is the colder, saltier Bering Summer Water (Itoh, Pickart, et al., 2015; Pickart, Nobre, et al., 2019). The latter water mass contains some amount of Anadyr Water (Coachman, 1967) and can also include some modified Remnant Winter Water (Gong & Pickart, 2016), hence it is higher in nutrients than the Alaskan Coastal Water. In addition to these Pacific-origin waters, Atlantic Water is periodically upwelled into Barrow Canyon during northeasterly wind events

when the flow is directed up-canyon (Ladd et al., 2016; Pickart, Nobre, et al., 2019; Pisareva, Pickart, Lin, et al., 2019; Weingartner, Potter, et al., 2017).

In this study, we seek to explain why the central part of Barrow Canyon contains exceptionally high values of benthic macrofaunal biomass. We demonstrate that the dynamics of the canyon flow results in strong vertical pumping of phytoplankton and oxygen to the seafloor. We further show that the temporal changes in the pumping, in conjunction with time variation in the phytoplankton entering the canyon, results in a variable supply of carbon to the seafloor both on monthly timescales as well as interannually. We begin the study with an observational description of the canyon flow and properties using repeat shipboard sections taken over a number of years. We then analytically specify the horizontal flow field, fashioned after the observations, and solve for the vertical velocity using the quasi-geostrophic omega equation. This, together with the use of a passive tracer, demonstrates that vertical pumping takes place in the canyon. Finally, we devise a proxy for the pumping and construct a time series of carbon supply to the canyon in order to investigate the time-varying signals.

2. Data and Methods

2.1. Repeat Shipboard Sections of Physical Parameters

Between 2009 and 2019, 11 shipboard sections were occupied across the central part of Barrow Canyon. The section is known as the Distributed Biological Observatory transect #5 (DBO5), and consists of 10 stations nominally spaced 5 km apart (Figure 1b). The DBO is a community-led effort to collect time series of physical, biophysical, and biological parameters at key locations in the Pacific-Arctic region (Moore et al., 2018). Eight sections have been identified (DBO1-8), from the northern Bering Sea to the Canadian Beaufort Sea, corresponding to regions of enhanced biological activity. The goal is to have research vessels occupy one or more transects when they pass through the various regions, as dictated by time and interest, and thereby build a climate-ecosystem time series. Measurements span from the basic physical variables (e.g., temperature, salinity) to chemical and biological quantities in the water column and benthos. The pilot phase of DBO began in 2010, and since that time vessels from six nations have contributed to the database (https://www.pmel.noaa.gov/dbo/).

The DBO5 crossings analyzed here were all carried out on the USCGC *Healy*, occupied between the months of July and October (Table 1). Two of the realizations occurred during upwelling conditions (reversed flow in the canyon) and are not considered in this study. The hydrographic data were collected using a Sea-Bird 911plus conductivity-temperature-depth (CTD) system. The temperature and conductivity sensors were calibrated at Sea-Bird prior and subsequent to each field season. On most of the cruises bottle salinity data were taken in order to perform an in situ calibration of the conductivity sensors (the bottle data were taken on deep casts in the Canada Basin). When this was not possible, we statistically compared the dual sensor data to estimate the uncertainty (see Pickart, Pratt, et al., 2010 for details). Overall, the temperature and practical salinity accuracies are taken to be 0.002°C and 0.008, respectively. The oxygen data were collected using a Sea-Bird SBE43 sensor, and the fluorescence data were obtained using a WetLabs ECO-AFL/FL instrument. These data were not calibrated, but the signals of interest are clear.

The velocity data used in the study were collected using *Healy's* hull-mounted 150 kHz Ocean Surveyor acoustic Doppler current profiler (ADCP). The data were processed using University of Hawaii's Common Ocean Data Access System processing code (http://currents. soest.hawaii.edu). The barotropic tidal signal was removed using the Oregon State University tidal model (http://volkov.oce.orst.edu/tides; Padman & Erofeeva, 2004). For details, the reader is referred to Pickart, Moore, et al. (2016).

Vertical sections of the different hydrographic and computed variables (such as potential vorticity) were constructed using Laplacian-Spline interpolation, with a grid spacing of 2.5 km in the horizontal and 2.5 m in the vertical. Absolute geostrophic velocities were computed using the gridded sections of dynamic height to compute relative geostrophic velocity sections. These were subsequently referenced using similarly gridded sections of cross-track ADCP velocity.

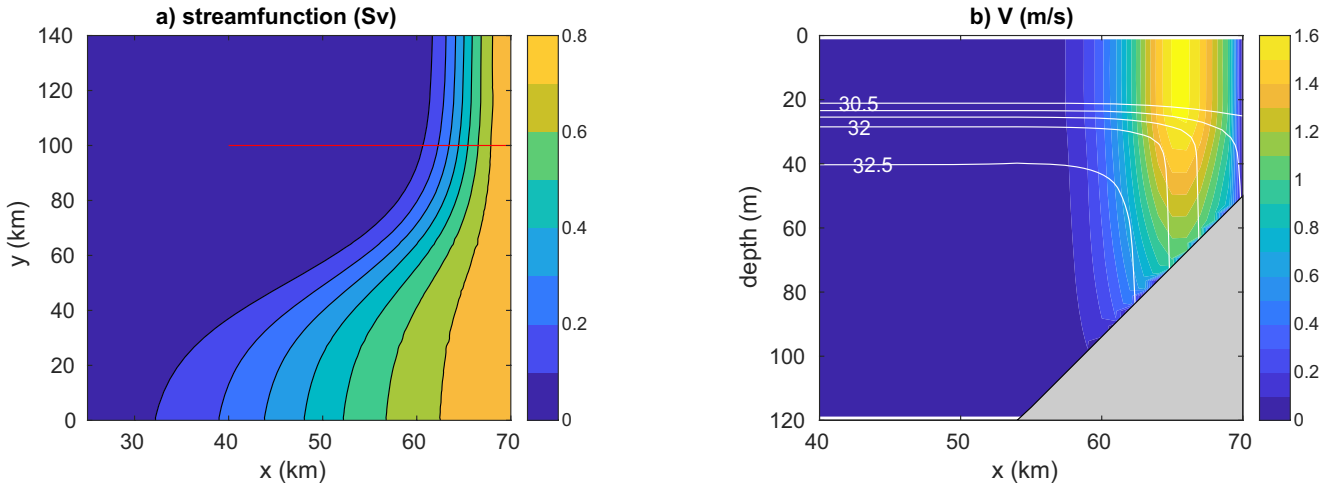

Figure 4. (a) Transport stream function, and (b) meridional velocity (color) overlain by salinity (contours) at $y = 100$ km (red line in a), depicting the geostrophic velocity field used to force the omega Equation 1.

2.2. Wind Data

We used the wind time series from the meteorological station in Utqiaġvik, AK, obtained from the National Climate Data Center of the National Oceanic and Atmospheric Administration (http://www.ncdc.noaa.gov/). The weather station is located close to the DBO5 line, and has been used in many Barrow Canyon studies (e.g., Pickart, Nobre, et al., 2019; Pisareva, Pickart, Lin, et al., 2019). The data have been quality controlled and interpolated to one-hour temporal resolution (see Pickart et al., 2013). The data during the period of 2003–2018 were used to be consistent with the MODIS ocean color data.

2.3. Benthic Data

The macrofaunal benthic data from the Barrow Canyon hotspot were collected over many cruises on multiple ships between 1999 and 2015 using a weighted 0.1 m^2 van Veen grab, sieved through a 1 mm screen, preserved, and returned to land for processing (see Grebmeier, Frey, et al. (2018) for detailed methods and J. M. Grebmeier and Cooper (2020) for a description of the macrofaunal data set).

2.4. Ocean Color Data

Satellite derived chlorophyll *a* (Chl *a*) was obtained for the time period 2003–2018 from the NASA Goddard Space Flight Center, Ocean Ecology Laboratory, Ocean Biology Processing Group (doi:data/10.5067/AQUA/MODIS/L3B/CHL/2018) were mapped to a common polar stereographic projection with 4 km resolution.

2.5. Vertical Velocities Using the Quasi-Geostrophic Omega Equation

Vertical motions in the coastal ocean are often forced by the interaction of wind-driven Ekman transports and the coast or bottom boundary layer. We argue instead that in Barrow Canyon strong downwelling results from the dynamics of the canyon throughflow. This is most easily illustrated by consideration of the quasi-geostrophic omega equation to solve for the vertical velocity field in a flow specified after the observed flow through Barrow Canyon. We then use this three-dimensional velocity field to advect a passive tracer representative of the phytoplankton source to demonstrate the mechanism leading to the Barrow Canyon hotspot.

The quasi-geostrophic omega equation is a diagnostic equation for the vertical velocity field in terms of the geostrophic velocity and the density field (Hoskins et al., 1978),

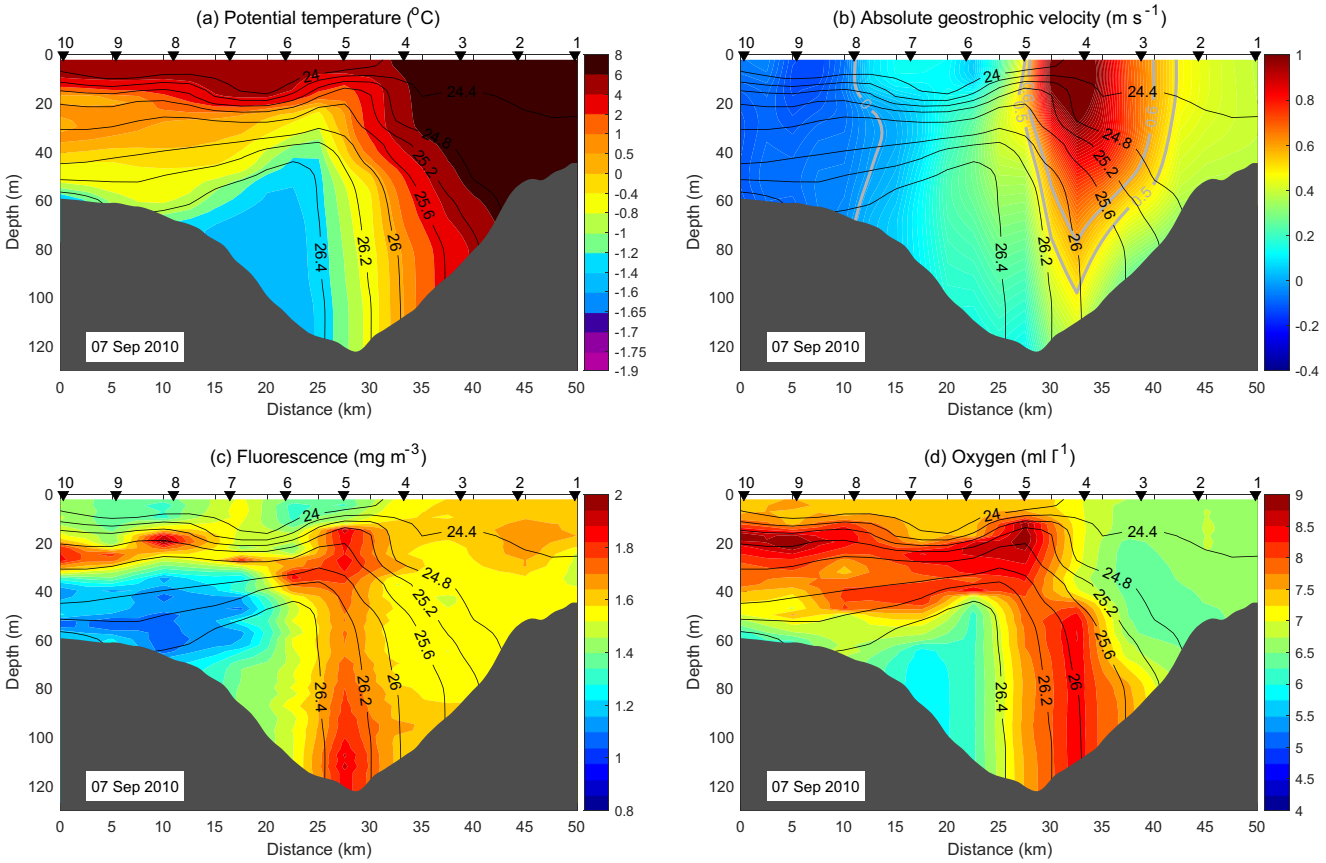

Figure 5. Vertical sections of (a) potential temperature (°C), (b) absolute geostrophic velocity (m s^{-1}), (c) fluorescence (mg m^{-3}), and (d) oxygen (ml l^{-1}) from the September 7, 2010 occupation of the DBO5 line. The contours are potential density (kg m^{-3}). Station positions/names are marked along the top.

$$N^2\nabla^2 w + f^2\frac{\partial^2 w}{\partial z^2} = 2\nabla\cdot\bar{Q}\,, \tag{1}$$

where

$$\nabla^2 = \frac{\partial}{\partial x^2} + \frac{\partial}{\partial y^2}$$

The zonal, meridional, and vertical distances are x, y, and z. The vertical velocity is forced by the vector

$$\bar{Q} = \frac{g}{\rho_0}\left(\frac{\partial u_g}{\partial x}\frac{\partial \rho}{\partial x} + \frac{\partial v_g}{\partial x}\frac{\partial \rho}{\partial y}, \frac{\partial u_g}{\partial y}\frac{\partial \rho}{\partial x} + \frac{\partial v_g}{\partial y}\frac{\partial \rho}{\partial y}\right) \tag{2}$$

The zonal and meridional geostrophic velocities are given by u_g and v_g, w is the vertical velocity, f is the Coriolis parameter (assumed constant), and N is the Brunt-Väisälä frequency, $\sqrt{-(g/\rho)(\partial\rho/\partial z)}$, where g is the gravitational acceleration and ρ is the density. The reference density is ρ_0. Solving the omega equation provides an estimate of the vertical velocity given the forcing function Q.

The essential features of the circulation leading to the vertical pumping, which need to be represented in this idealized configuration, are that the flow is stratified and it accelerates as it enters the canyon. We solve the omega equation in a domain that extends 140 km in the along-flow direction y and 70 km in the cross-flow direction x. The current is defined to flow parallel to the bottom topography and be in geostrophic balance. The topography slopes linearly from 50 m at the right-hand wall to 120 m over a width L and

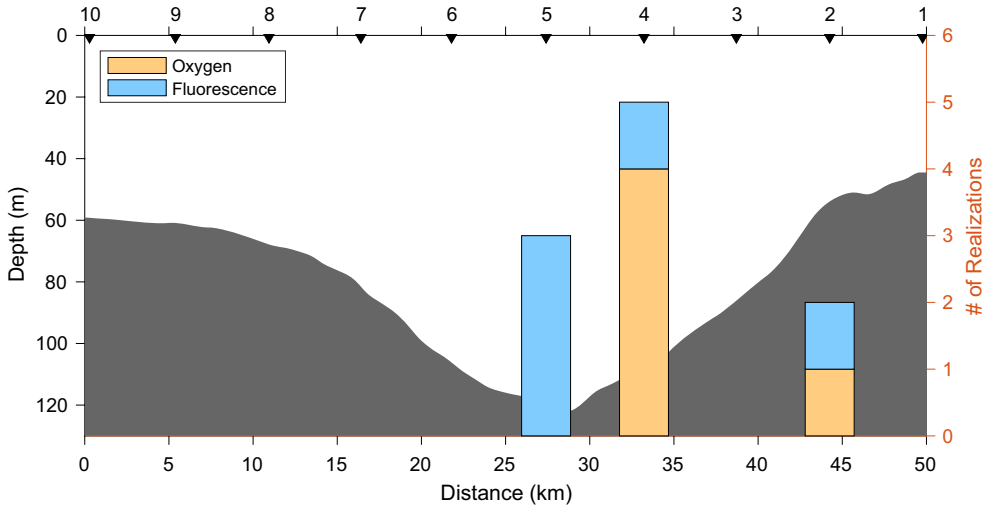

Figure 6. Locations along the DBO5 line where the fluorescence and oxygen plumes intersect the bottom. The number of realizations at each station location is tabulated. Station positions/names are marked along the top.

is flat beyond that distance. The width of the sloping topography varies from 70 km at $y = 0$ km to 14 km at $y = 140$ km, following a hyperbolic tangent function in y with a meridional transition scale of 30 km. Note that this configuration only represents the eastern side of Barrow Canyon, as the flow in question is banked against this flank (see the observations in Section 3). The topography and stream function so defined are reflective of the weaker flow feeding the canyon from the broad Chukchi shelf (Weingartner, Potter, et al., 2017), with an acceleration over a similar distance as the length of the canyon.

The velocity is in geostrophic balance with the density field, which is controlled by salinity through a linear equation of state as $\rho = \rho_0 + \beta\left(S - S_0\right)$, where β is the haline contraction coefficient and ρ_0 and S_0 are the reference density and salinity (all salinities are in Practical Salinity Units). The salinity is defined to have a halocline in the vertical and a front in the horizontal. The vertical stratification is dominated by the halocline with a change in salinity of 1.75 centered at 25 m depth. Below this the stratification is weak with $N^2 = 1 \times 10^{-5}\ \mathrm{s}^{-2}$, and above this is a mixed layer extending to the surface. The horizontal density front has a change in salinity of 1 across the front, is centered over the 70 m isobath, and decays across the topography with a hyperbolic tangent between the 50 and 90 m isobaths. A barotropic mode is added that is 20% of the baroclinic shear between the bottom and the surface which, for this case, is on the order of 0.2 m s^{-1} at the core of the jet. The velocity and density fields so configured are shown in Figure 4. Note that the stream function in Figure 4a shows the pattern of the bottom topography since the flow follows the isobaths.

The omega Equation 1 is solved on a grid with 1 km horizontal spacing and 2.5 m vertical spacing. The boundary condition at the surface is $w = 0$, while the boundary condition at $z = 120$ m is $\partial w / \partial z = 0$. The equation is solved without consideration of the sloping bottom. It is assumed that a narrow bottom boundary layer exists that will satisfy the no-normal flow boundary condition there.

3. Observational Evidence of Vertical Pumping in Barrow Canyon

As demonstrated by Lin, Pickart, McRaven, et al. (2019) using a historical database of shipboard ADCP data, the flow in Barrow Canyon during summer and early-fall is northward for all wind directions except northeasterly (when upwelling occurs if the winds are strong enough). As mentioned above, two of our 11 crossings were taken during upwelling conditions when the flow was reversed to the south; these sections are not considered in this study. Figure 5 shows the conditions in the canyon during the DBO5 occupation on September 7, 2010. At this time, warm Alaskan Coastal Water was present on the shallow part of the canyon's eastern flank, while cold Remnant Winter Water was located above the bottom on the canyon's western flank (Figure 5a). This configuration of water masses is typical for early fall (Pickart, Nobre, et al., 2019). The northward flow was dominated by the ACC, coincident with the density front in the

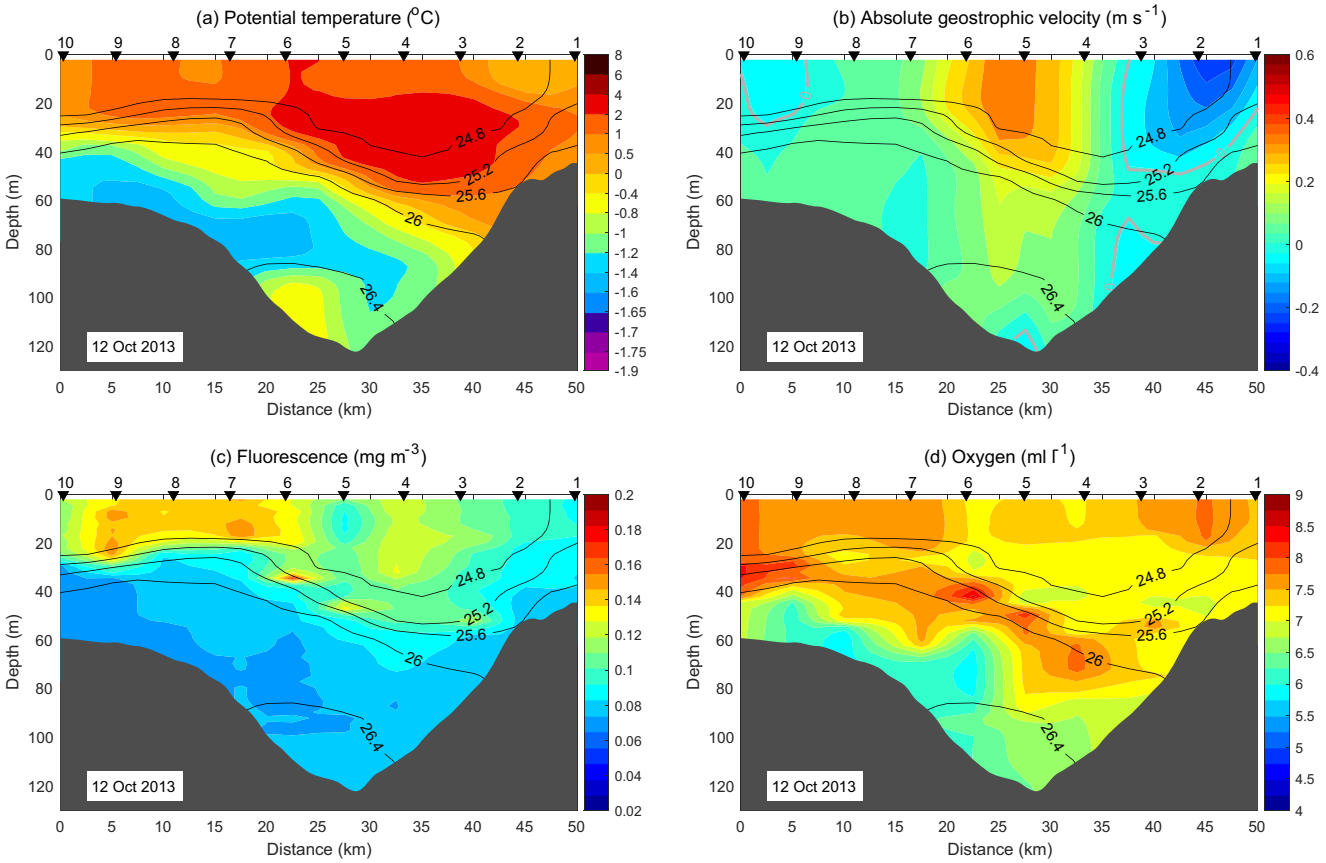

Figure 7. Same as Figure 5 except for the October 12, 2013 occupation of the DBO5 line.

canyon (Figure 5b). Notably, the isopycnals in the front were almost vertical and intersected the bottom in the deep part of the canyon. Associated with this was a plume of high fluorescence that extended from the pycnocline to the seafloor (Figure 5c), and a similar plume of high oxygen (Figure 5d).

This occupation suggests that carbon can be fluxed to the bottom of Barrow Canyon in the vicinity of the benthic macrofaunal hotpot (Figure 2). It is highly unlikely that this was due to local gravitational sinking of the phytoplankton for two reasons. First, the typical rate of settling (1 m day^{-1}, Bannon & Campbell, 2017; Eppley et al., 1967) means that it would take months to reach the bottom from the depth of the pycnocline. The speed of the ACC at these depths is on the order of 0.5 m s^{-1}, which implies a two days transit for the water to travel the 100 km distance from the head of the canyon to the DBO5 line. Second, the presence of the oxygen plume implies strong vertical advection and/or strong vertical mixing at this location (since oxygen is not subject to gravitational sinking). As noted above, there is no reason to believe that the turbulent mixing in the canyon is localized to the region of the benthic hotspot.

One sees in Figure 5 that the oxygen plume is located to the right of the fluorescence plume (the former was measured at station 4, while the latter was measured at station 5). This happened in three out of the four instances when these plumes were measured near the bottom of the canyon (Figure 6). This can be explained by the fact that, as blooms develop, the enhanced oxygen signals are found shallower in the water column than the highest concentrations of phytoplankton, due to the settling of the phytoplankton. As such, the oxygen signature will correspond to lighter isopycnals, which are found more shoreward in the density front within the canyon. Note in Figure 6 that, for one of the realizations, the two plumes were located far upslope near the eastern edge of the canyon. During this occupation, the ACC was located very far onshore, and the 25.5 kg m^{-3} isopycnal intersected the bottom between stations 1 and 2 near 50 m depth, compared to Figure 5 where this isopycnal grounded near 90 m. For these reasons, we exclude this occupation in the analysis below (it is an outlier in other respects as well).

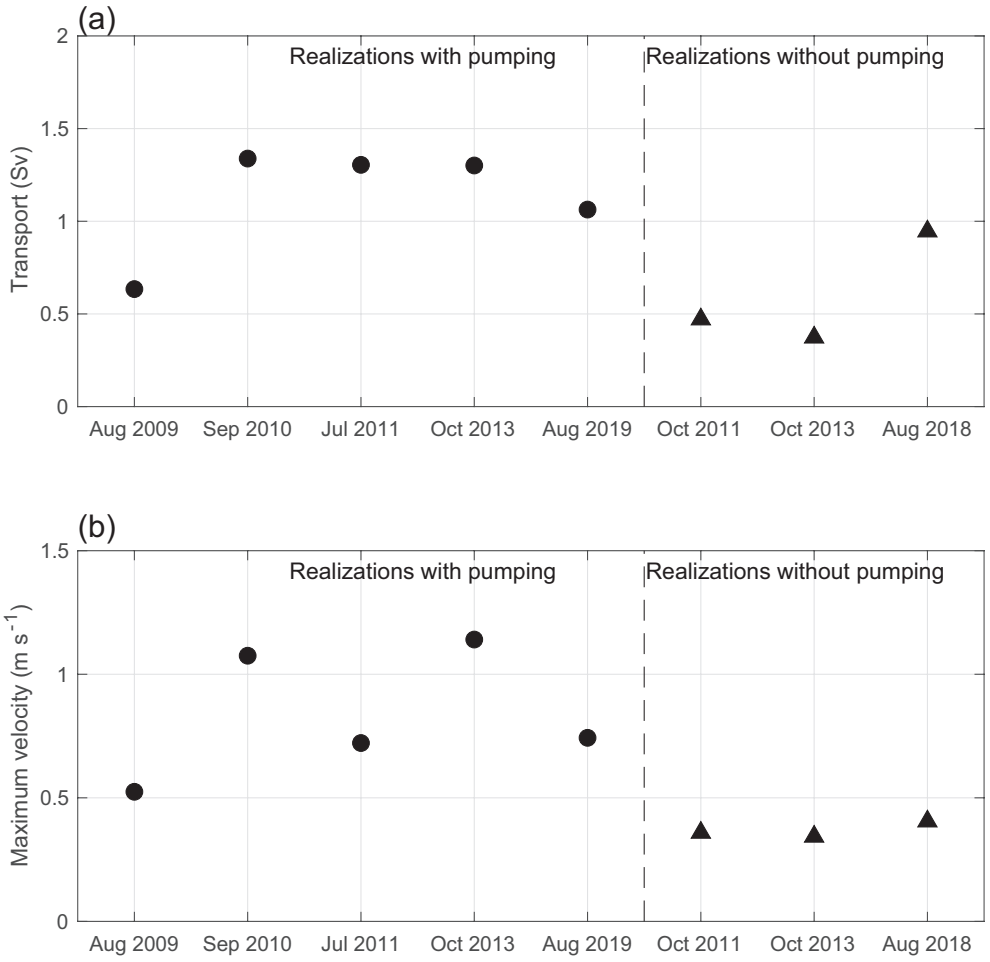

Figure 8. Comparison between the pumping realizations and nonpumping realizations for (a) volume transport (Sv) of the ACC, and (b) peak velocity (m s^{-1}) of the ACC.

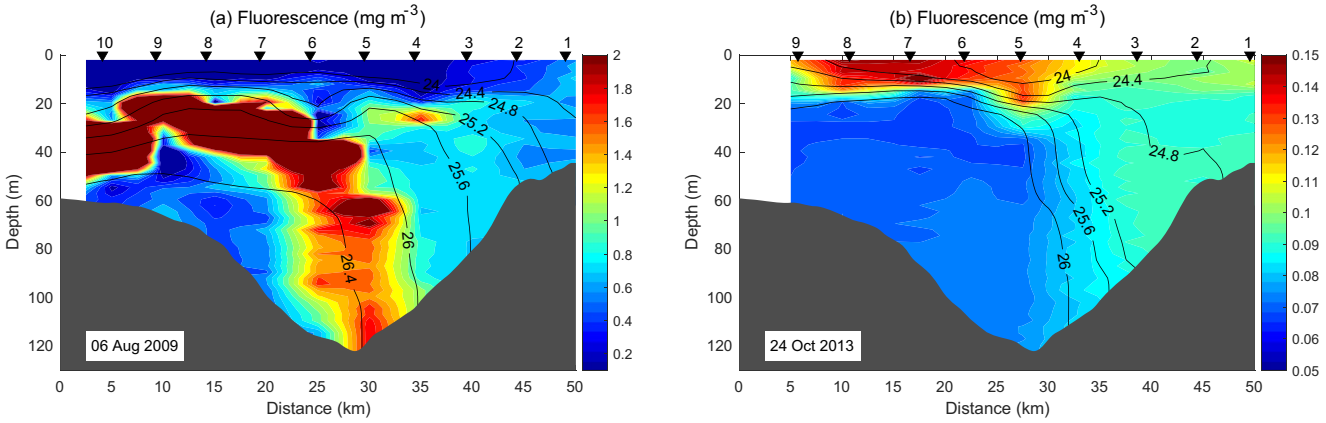

Figure 9. Vertical sections of fluorescence (color, mg m^{-3}), overlain by density (contours, kg m^{-3}) for (a) one of the pumping realizations when there was a fluorescence plume (August 6, 2009), and (b) the only pumping realization when there was no such plume (October 24, 2013). Station positions/names are marked along the top.

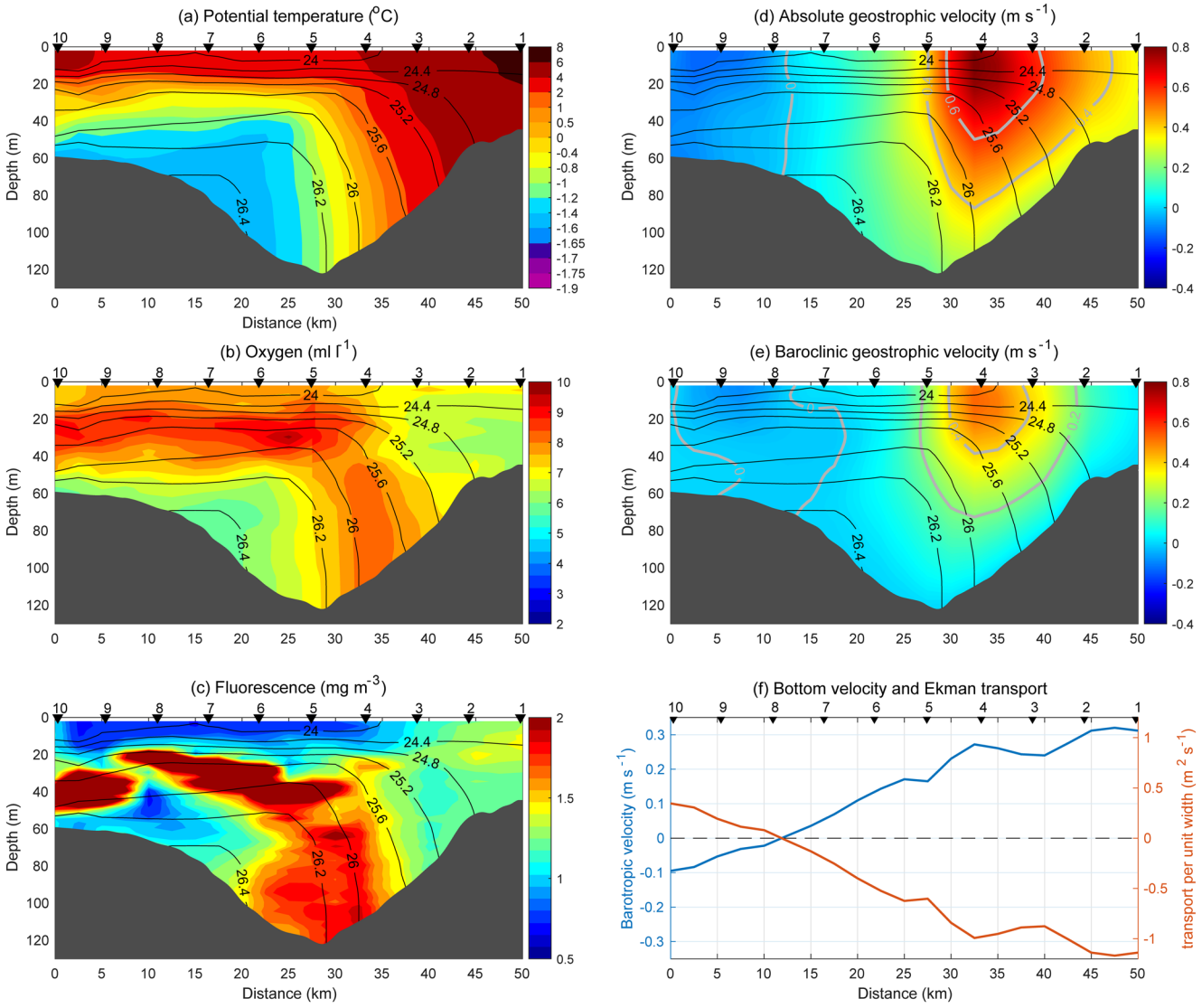

Figure 10. Composite sections for the pumping realizations. (a) Potential temperature (color, °C) overlain by potential density (contours, kg m^{-3}). (b) Oxygen (color, ml l^{-1}). (c) Fluorescence (color, mg m^{-3}). (d) Absolute geostrophic velocity (color and thick gray contours, m s^{-1}). (e) Baroclinic geostrophic velocity (color and thick gray contours, m s^{-1}). (f) Bottom velocity (blue curve, m s^{-1}) and bottom Ekman transport per unit width (red curve, m^2 s^{-1}). Station positions/names are marked along the top.

In contrast to the crossing described above, Figure 7 shows the October 12, 2013 section which is markedly different. During this realization, the predominant water mass on the eastern side of the canyon in the upper layer is Bering Summer Water, although the deep signature of Remnant Winter Water at depth on the western side of the canyon is similar to the previous section (Figure 7a). Another difference is that the ACC is substantially weaker in the October 12, 2013 section (Figure 7b), with a peak speed of ~0.3 m s^{-1} (vs. > 1 m s^{-1} for the previous realization). The most notable difference, however, is in the density field and the biochemical signals. In particular, the isopycnals are much more gently sloped, and even slope upward toward the coast at the eastern end of the canyon. As such, there is no vertically aligned front, and no vertical plumes of fluorescence and oxygen (Figures 7c and 7d). Hence, in this realization, the benthic macrofaunal hotspot is not subject to a vertical flux of carbon.

In all, five of the DBO5 sections contained a strong density front centered in the deep part of the canyon, with isopycnals sloping nearly vertically. In four of these realizations, downward plumes of fluorescence and oxygen—reaching the sea floor—coincided with the front (akin to the example in Figure 5). By contrast,

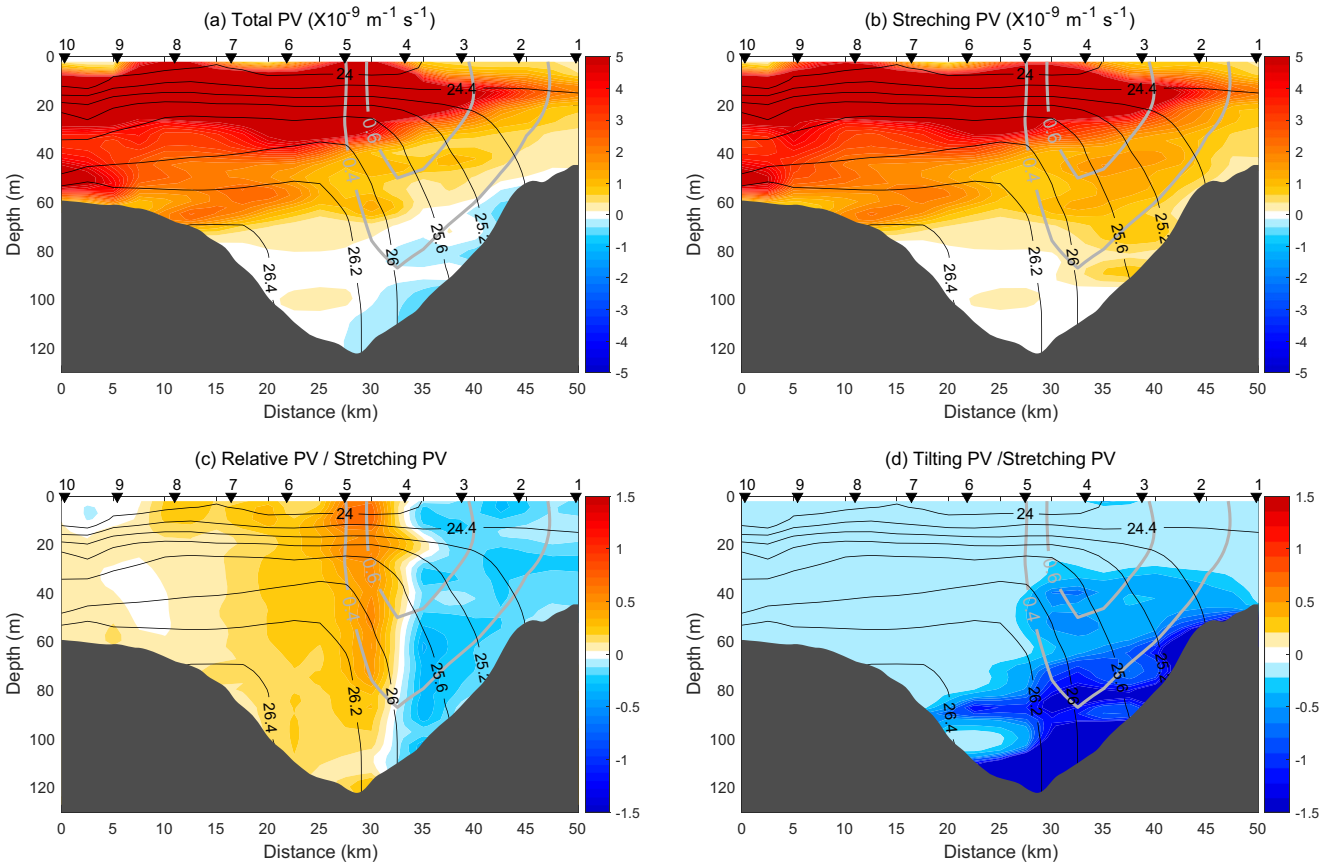

Figure 11. Composite sections of potential vorticity for the pumping realizations. (a) Total potential vorticity (color, $m^{-1}\ s^{-1}$) overlain by potential density (contours, kg m^{-3}). (b) The planetary stretching vorticity. (c) The relative vorticity and (d) tilting vorticity, both normalized by the stretching vorticity. Contours of the absolute geostrophic velocity are shown (thick gray lines, m s^{-1}). Station positions/names are marked along the top.

three sections were characterized by more gently sloping isopycnals that did not intersect the deep part of the canyon, but instead grounded at shallow depths on the eastern flank of the canyon or did not ground at all within the canyon domain (akin to the example in Figure 7). In these three cases, there were no fluorescence/oxygen plumes. As noted above, two of the remaining three sections corresponded to upwelling, and the third remaining section had an anomalous configuration of the ACC. This information is summarized in Table 1.

We refer to the five realizations with a strong density front as the pumping cases and the three realizations with a weak density front as the nonpumping cases. What dictates these two states? We note that pumping was observed in each month from July to October (Table 1), while the nonpumping cases were in August and October. Hence the particular month of the warm season seems not to matter. Additionally, the type of water masses in the canyon does not appear to play a role. A composite T/S diagram (not shown) reveals that each of the four Pacific water masses were present in both cases, in roughly equal amounts. Instead, the pumping scenario appears to be related to the strength of the ACC. Figure 8 contrasts the volume transport and peak velocity of the ACC for each of the realizations. This implies that a strong ACC favors pumping: the mean transport for the pumping cases is 1.15 ± 0.31 Sv vs. 0.60 ± 0.31 Sv for the nonpumping cases, and the maximum ACC speed is 0.87 ± 0.27 m s^{-1} for the former vs. 0.39 ± 0.04 m s^{-1} for the latter. This makes sense in that the strong front results in a larger thermal wind signature. Wind is also a factor, which is addressed below in Section 5.

As mentioned earlier, one of the pumping realizations was not associated with a fluorescence or oxygen plume (the October 24, 2013 occupation, Table 1). This realization is shown in comparison with another of the plume realizations in Figure 9. There is nothing special about the configuration of the density front

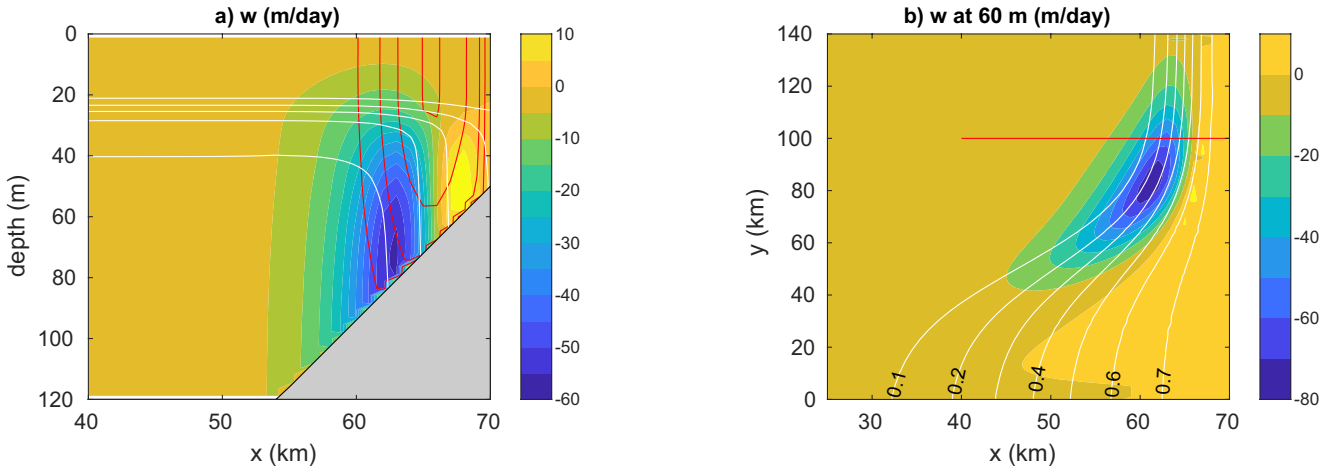

Figure 12. Vertical velocity (color) from the omega equation in (a) the vertical plane and (b) the horizontal plane at 60 m depth. The location of the vertical section is marked in (b) by the red line. In (a) the meridional velocity of the jet and the isohalines of the front are denoted by the red and white contours, respectively. In (b) the white contours are the transport stream function.

in this case, and the transport and maximum velocity of the ACC were comparable to other pumping cases (Figure 8). What sets this realization apart from the others is that this is the only case where the Chl *a* maximum was in the surface layer rather than in the pycnocline (Figure 9). We demonstrate below in Section 4 that the depth at which the bloom resides in the water column is critical for whether or not a downward plume develops.

Using the five pumping realizations, we created composite vertical sections (excluding the nonplume case for the oxygen and fluorescence composites.) This shows the canonical pumping scenario (Figure 10). The ACC, transporting predominantly Alaskan Coastal Water, is located above the eastern flank of the canyon flowing strongly to the north, coincident with a strong density front. A plume of fluorescence extends to the bottom, with an oxygen plume a bit shoreward of this. Although the fluorescence plume is not always centered at the deepest part of the canyon, the largest values of benthic macrofaunal biomass are always measured there across seasons. This might be due to the flow in the bottom Ekman layer. We estimated the bottom stress using a linear drag law, $\tau_b = \rho_0 r v_b$, where $r = 5{\times}10^{-4}$ m s^{-1} (Lentz & Winant, 1986), ρ_0 is the reference density, and v_b is the along-canyon geostrophic velocity at the top of the Ekman layer. This was taken to be the velocity 10 m above the bottom from Figure 10d. The cross-slope bottom Ekman transport per unit width was then computed as $\tau_b / f\rho_0$. One sees that the transport is directed down the slope on the eastern side of the canyon (Figure 10f), which would tend to flux the near-bottom carbon toward the location of the hotspot. For a 10 m thick bottom Ekman layer, the cross-canyon velocity is ~0.05 m s^{-1}, which would advect parcels ~10 km in two days, enough to reach the deep part of the canyon.

To calculate the portion of the ACC associated with the density front, we subtracted the bottom velocity at each location from the full velocity profile. The resulting field can be considered the baroclinic component (i.e., the velocity referenced to the bottom, Figure 10e). The transport of the baroclinic ACC is 0.61 vs. 1.16 Sv for the full field, with a maximum velocity of 0.59 m s^{-1} vs. 0.80 m s^{-1}. The barotropic velocity is fairly uniform across the eastern flank of the canyon, ~0.20 m s^{-1}. On the western shoulder of the canyon the flow is to the south (both the full flow and the baroclinic flow). This is likely the signature of the anti-cyclonic circulation around the north side of Hanna Shoal that ultimately retroflects and drains into the canyon (Figure 3).

It is of interest to consider the potential vorticity structure of the flow in Barrow Canyon for the pumping scenario. The Ertel potential vorticity (Π) can be written as (Pickart, Torres, & Fratantoni, 2005; Spall & Pedlosky, 2008):

$$\Pi = -\frac{f}{\rho_0}\frac{\partial \rho}{\partial z} + \frac{1}{\rho_0}\frac{\partial v}{\partial x}\frac{\partial \rho}{\partial z} - \frac{1}{\rho_0}\frac{\partial v}{\partial z}\frac{\partial \rho}{\partial x}, \tag{3}$$

where x is the cross-canyon direction, positive toward the coast; z is the vertical coordinate, positive upward; ρ is the density (ρ_0 is the reference density noted above); and v is the along-canyon velocity, positive northwards. Π has three components: (1) the planetary stretching term dictated by the vertical stratification and the rotation of the Earth; (2) the relative vorticity term; and (3) the tilting term. It is instructive to normalize the second and third terms by the planetary stretching term, which converts these terms to a Rossby number and a so-called shear Rossby number, respectively (Lin, Pickart, Jochumsen, et al., 2020).

We created a composite vertical section for the pumping realizations of Π and its three components (Figure 11). In the upper layer, the potential vorticity is dominated by the stretching term, due to the large stratification of the pycnocline. The Rossby number of the ACC is quite large, with a maximum value of ~0.6. During two of the crossings (September 2010 and October 2013) the Rossby number was ~0.9. This suggests that the current can be highly nonlinear and subject to barotropic instability. Π also satisfies the condition for baroclinic instability (a change in sign of $\partial\Pi / \partial x$ with depth; Pedlosky, 1979), although the sloping bottom will tend to stabilize the front (Blumsack & Gierasch, 1972). This condition was also noted using data from a synoptic survey of the canyon (Pickart, Torres, & Fratantoni, 2005). The outflow from Barrow Canyon is known to be quite turbulent at times (MacKinnon et al., 2020) and coherent eddies have been observed just seaward of the canyon mouth (Pickart & Stossmeister, 2008). Our composite Π fields suggest that hydrodynamic instability of the ACC contributes to this variability.

Another notable feature of the potential vorticity in the pumping composite is the region of strong negative tilting vorticity, associated with the steeply sloped isopycnals of the density front (Figures 11d). Values of the shear Rossby number exceed −1, which together with the strong negative relative vorticity on the anti-cyclonic side of the ACC, lead to a region of negative total potential vorticity (Figures 11a). Such a condition can lead to symmetric instability (e.g., Lin, Pickart, Jochumsen, et al., 2020), which can reach finite amplitude in a matter of hours (Brearley et al., 2012). This implies that, when the ACC is strong and the associated density front is sharp, the outflow of the canyon is subject to strong mixing. This in turn could lead to entrainment of ambient water and an increase in the outflowing transport.

4. Dynamics of the Pumping

The omega equation is now solved for a flow structure typical of the ACC in Barrow Canyon. The velocity and density field defining the forcing vector Q is shown in Figure 4. The transport stream function (this is also the pattern for the bottom topography) has a maximum value of 0.8 Sv. Although the transport is conserved following the flow, the horizontal velocity increases from the southern end of the domain, where the topography and flow are broad, to the northern end of the domain, where the topography is narrow and the current becomes more confined. This represents the progression of flow into Barrow Canyon. The meridional velocity and salinity along a section at $y = 100$ km are shown by the red and white contours, respectively, in Figure 12a. The gradient in salinity over the 70 m isobath supports a baroclinic jet with maximum velocity of 1.5 m s^{-1}. The velocity and salinity (i.e., density) structure are broadly consistent with the data shown in Figures 5 and 10. The primary results from this idealized model are not overly sensitive to the details of the velocity and density structure, but are sensitive to the stratification and strength of the front, as described further below.

The vertical velocity derived from the omega equation along the section at $y = 100$ km is shown in color in Figure 12a. The downwelling is weak near the surface and increases toward the bottom, especially so below the halocline. The maximum downwelling of ~60 m day^{-1} is located at the bottom on the cyclonic side of the jet. There is also weaker upwelling on the anticyclonic side of the jet. The lateral structure of the downwelling plume is indicated by the vertical velocity at 60 m depth (Figure 12b). The downwelling is concentrated along the cyclonic side of the front in the region where the isobaths are converging and the flow is accelerating. The maximum downwelling rate at this depth is close to 80 m day^{-1}.

A more complete picture of the vertical transport driven by this downwelling cell is provided by integration of a passive tracer using the three-dimensional velocity field (u_g, v_g, w). Two different initial conditions for the tracer are considered. In the first case, the tracer is initialized as a horizontally uniform layer centered at 30 m depth within the pycnocline, with a vertical decay scale of 10 m. This represents typical conditions in which the property plume was present in the observations (Figure 9a). In the second case, the tracer is

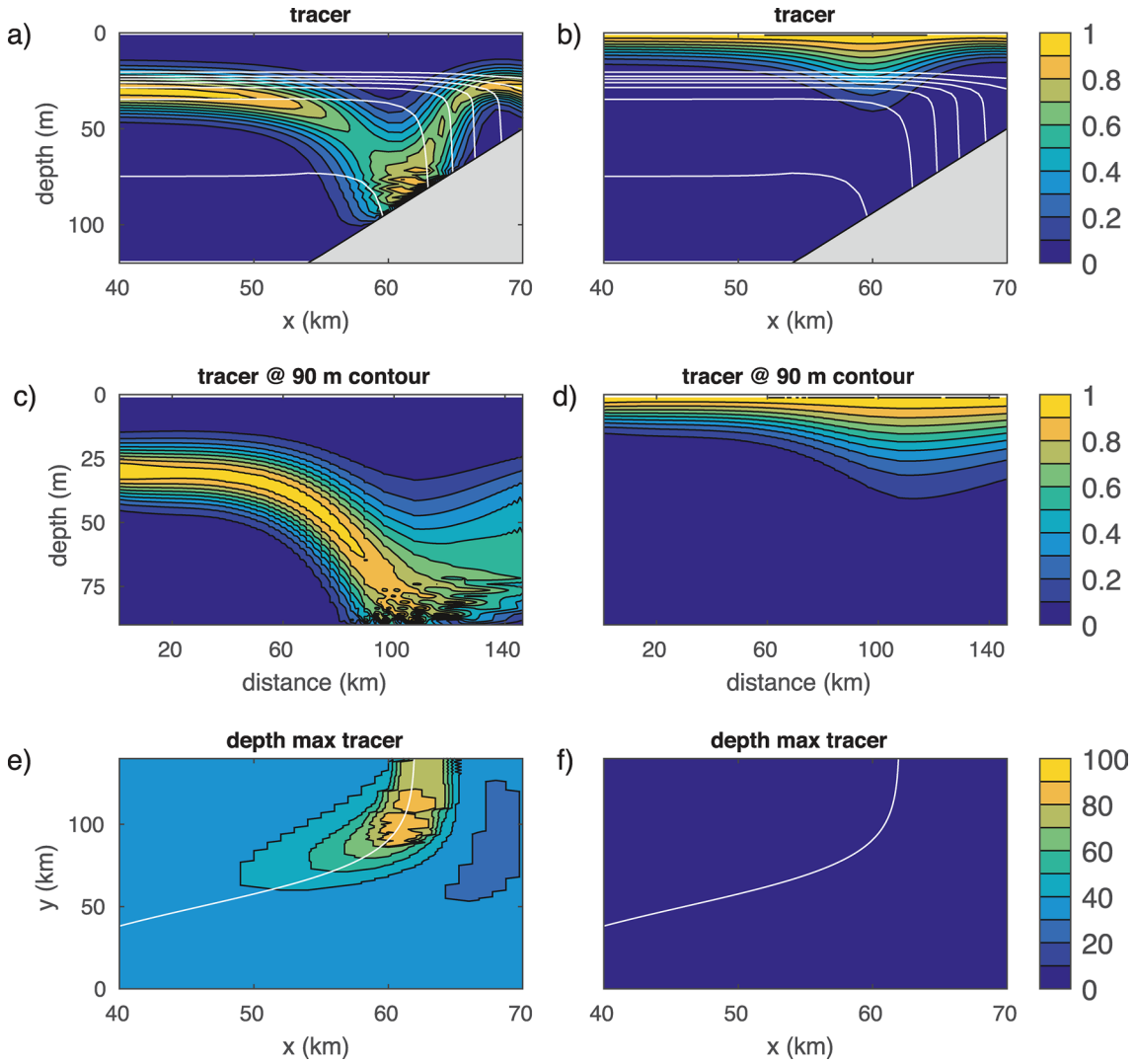

Figure 13. (a and b) Vertical section of the passive tracer at $y = 100$ km (see Figure 12b for the location of the section). (c and d) Depth-distance plot of the passive tracer along the 90 m isobath. (e and f) Depth of the maximum tracer, where the white line marks the 90 m isobath. The plots in the left-hand column are for the case when the initial tracer is introduced at 30 m. The plots in the right-hand column are for when the initial tracer is introduced at the surface.

initialized with its core at the surface, representing the case in which the flow and density front were strong but no plume developed (Figure 9b). The tracer is advected with the three-dimensional velocity field subject to Laplacian horizontal diffusion with a coefficient of 40 $m^2\ s^{-1}$ and a vertical diffusion coefficient of $2 \times 10^{-5}\ m^2\ s^{-1}$ for two days. The tracer at the inflowing boundary is held fixed at the initial condition.

The tracer along the section at $y = 100$ km for the subsurface initial condition after two days of integration is shown in Figure 13a. In this case, the tracer penetrates to the bottom on the cyclonic side of the jet, while the tracer on the anticyclonic side and to the west of the jet remain close to their initial conditions. The descent following the flow is indicated by the tracer as a function of depth and distance along the 90 m isobath, which marks the pathway of the cyclonic side of the front (Figure 13c). The tracer begins to descend about 60 km into the domain, which is where the topography begins to converge. The tracer plunges to the bottom as it passes through the region of maximum acceleration and reaches the 90 m isobath before the flow passes through the canyon. The shallow tracer at 140 km distance is partly left over from the initial conditions and partly advected from upstream. The localization of the tracer plume in the horizontal plane is indicated by the depth of the maximum tracer concentration (Figure 13e). The maximum penetration is always found close to the 90 m isobath (white contour) and the deepest penetration to 90 m is found on the

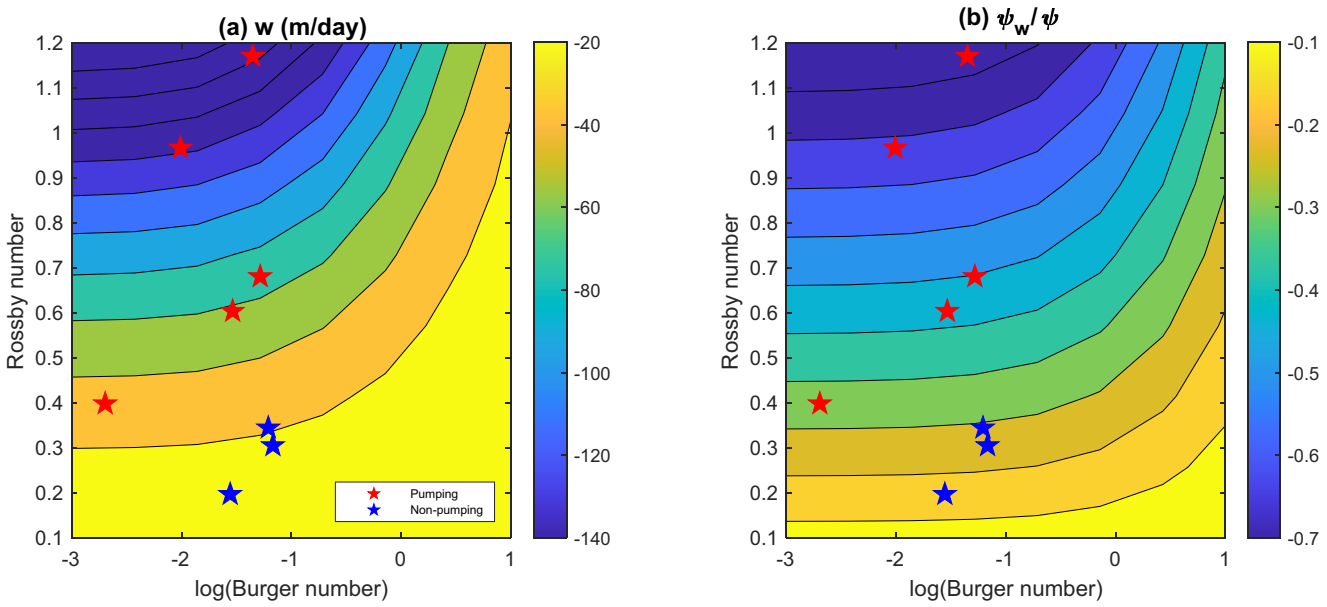

Figure 14. (a) Maximum downwelling and (b) ratio of the vertical transport to the horizontal transport at 60 m depth as a function of Rossby number and Burger number. The red (blue) stars mark the observed pumping (nonpumping) cases.

downstream side of the convergent topography. We note that the along stream localization of the pumped tracer is consistent with the benthic macrofaunal biomass data, which show that the Barrow Canyon hotspot is confined, in the along-canyon sense, to the region of the DBO5 transect (indeed, this is why the transect was chosen for the DBO program).

When the tracer is initialized at the surface the results are strikingly different. In this case, there is much less penetration (Figures 13b, 13d and 13f). The vertical velocity is weak near the surface because of the surface boundary condition. It is also difficult to advect tracer vertically through the halocline because stratification inhibits vertical motion. This is consistent with the observations that show no deep plume for the case in which the fluorescence was near the surface (Figure 9b), even though the physical conditions suggest that vertical pumping was active.

The above examples were chosen to represent conditions in Barrow Canyon typical of a strong ACC in order to elucidate the dynamics associated with the pumping of material to the canyon floor. However, the conditions in Barrow Canyon are highly variable on time scales of days to years, so it is instructive to understand how the state of the convergent flow dictates the manner in which tracers are subducted far below the halocline. A simple guideline is provided by a nondimensionalization of the omega equation using the following scaling:

$$\left(x,y,z\right) \propto \left(L_x,L_y,D\right) \quad \left(u_g,v_g,w\right) \propto \left(g\Delta\rho D \,/\, \rho_0 f_0 L_y, g\Delta\rho D \,/\, \rho_0 f_0 L_x, v_g D \,/\, L_y\right). \tag{4}$$

The width of the topography in the canyon is L_x, the along-flow convergence length scale is L_y, and D is the bottom depth. The horizontal velocities scale with the geostrophic velocity where $\Delta\rho$ is the density change across the front. The nondimensional vertical velocity then scales as

$$w \propto \frac{R}{B+1}, \tag{5}$$

where

$$R = v_g \,/\, f_0 L_x \; and \; B = N^2 D^2 \,/\, f_0^2 L_x^2 \tag{6}$$

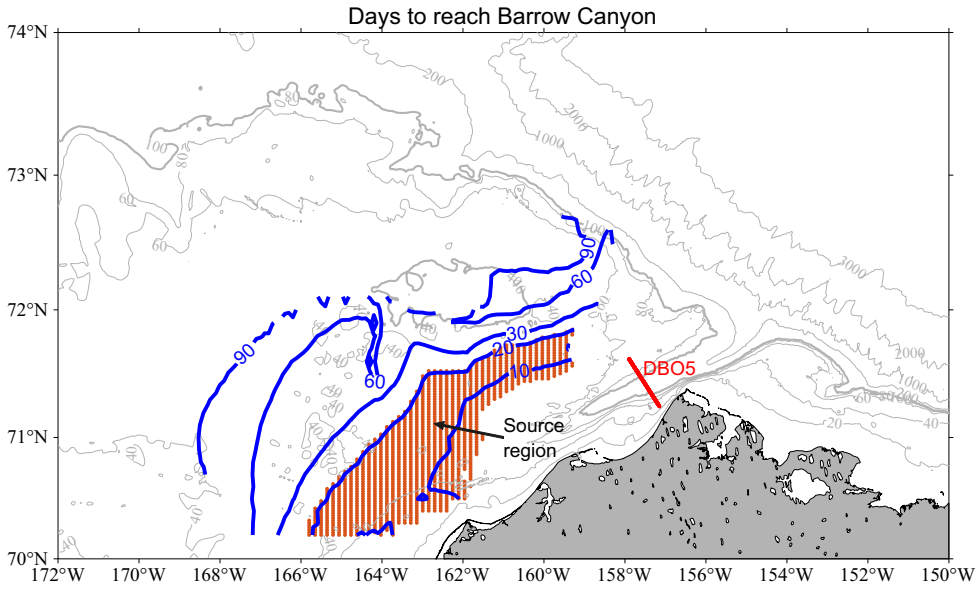

Figure 15. Map of elapsed time (in days, blue contours) for parcels to reach the DBO5 transect from the Chukchi shelf. The red hatching denotes the period of 7–21 days, corresponding to the source region of Chl *a* to the pycnocline in Barrow Canyon (see text for details).

R is the Rossby number of the flow through the canyon and B is the Burger number, which respectively represent the strength of the relative vorticity compared to Earth's rotation, and the width of the topography compared to the baroclinic deformation radius. Based on this scaling, the nondimensional downwelling increases linearly with Rossby number and becomes independent of stratification for $B << 1$ (weak stratification). Keep in mind that the vertical velocity is scaled with the horizontal velocity, which also increases linearly with R, so that the dimensional vertical velocity is expected to increase as R^2. Stratification begins to shut down the vertical motion when B becomes larger than order 1. This occurs when the internal deformation radius, ND / f, exceeds the lateral length scale of the topography, which in the present case is on the order of 15 km.

We solved the omega equation for a range of Rossby and Burger numbers, $0.1 < R < 1$ and $0.001 < B < 10$. The Rossby number was varied by modifying the change in salinity across the front, while the Burger number was varied by changing the background stratification N^2. The maximum downwelling at 60 m depth is shown as a function of R and B in Figure 14a. As anticipated by the scaling, the dimensional downwelling increases quadratically with increasing Rossby number and decreases with increasing Burger number. Downwelling for large R and small B approaches 150 m day^{-1}. In the figure, we have marked the values of R and B for each of the observational sections, where the Rossby number was taken to be the maximum absolute value in the section, and the Burger number is the average value beneath the pycnocline. The red symbols are the pumping cases and the blue symbols are the realizations without pumping.

The scaling and omega equation predict the general trend of large R and small B favoring pumping to the bottom. The observed conditions in Barrow Canyon are mostly dictated by the Rossby number, with little variation in stratification. We note that the transport stream function does not depend on the stratification, so the transport is a good proxy for the Rossby number.

The fraction of the transport in the flow through Barrow Canyon that downwells through 60 m depth is shown in Figure 14b. This increases linearly with Rossby number, as anticipated by the scaling (5). For large Rossby numbers over half of the horizontal transport downwells through the 60 m interface, significantly modifying the vertical structure of the flow with the potential to supply considerable phytoplankton to the seafloor. The vertical velocity adjusts very quickly (on the inertial time scale) to changes in the geostrophic flow field, so it is expected that the strength of downwelling and the supply of phytoplankton to the bottom of Barrow Canyon will vary strongly on synoptic to seasonal time scales.

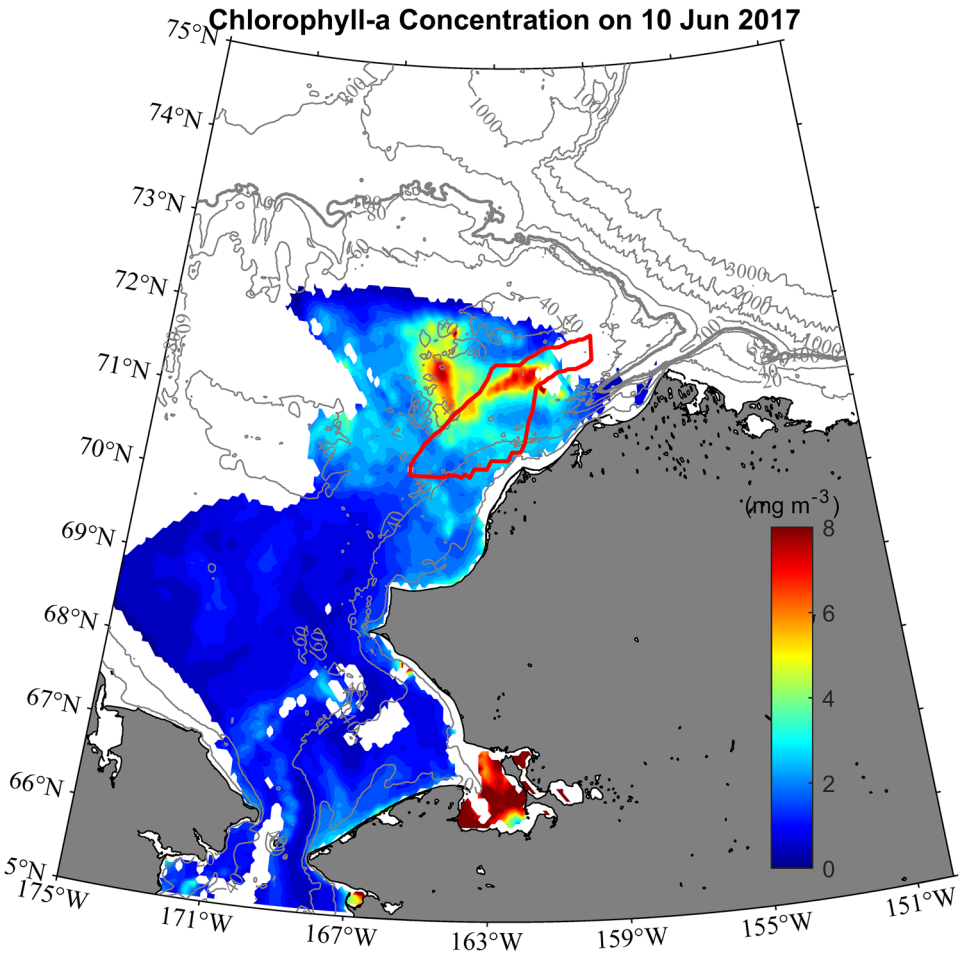

Figure 16. Chl *a* concentration (color) based on the MODIS image for June 10, 2017. The source region from Figure 15 is delineated by the red line.

5. Time Variation of the Carbon Supply to the Benthos

We now address time variation in the pumping, in conjunction with variability of the phytoplankton source, to assess the delivery of carbon to the bottom of Barrow Canyon.

The above results demonstrate that when the ACC is strong, material is efficiently pumped downward from the pycnocline. It is well known that the flow through the canyon is highly sensitive to the wind (e.g., Weingartner, Potter, et al., 2017). Lin, Pickart, McRaven, et al. (2019) compiled a composite data set of shipboard ADCP data in the northeastern Chukchi Sea from cruises conducted between 2003 and 2017 during the months of June and October. They determined that, unless the wind is blowing out of the northeast, the flow is always down-canyon. This suggests that we focus on the role of northeasterly winds in influencing the strength of the ACC and hence the pumping.

Using 2 years of mooring data from the head of Barrow Canyon, Pisareva, Pickart, Lin, et al. (2019) found that, once the northeasterly winds exceed 5 m s^{-1}, the canyon flow can reverse to the south and upwelling can commence. This is consistent with mooring data from the continental slope to the east of the canyon, where the Beaufort shelfbreak jet can reverse once the alongcoast winds exceed 4 m s^{-1} (Schulze & Pickart, 2012). Using shipboard hydrographic sections in Barrow Canyon, Pickart, Nobre, et al. (2019) found the strongest correlation between the northeasterly wind and upwelling signals in the data when they considered the wind over the 3-day period prior to the occupation of the section. Taking all of this into account, we defined a proxy to represent the strength of the ACC as follows. First, for each hourly data point in the 10

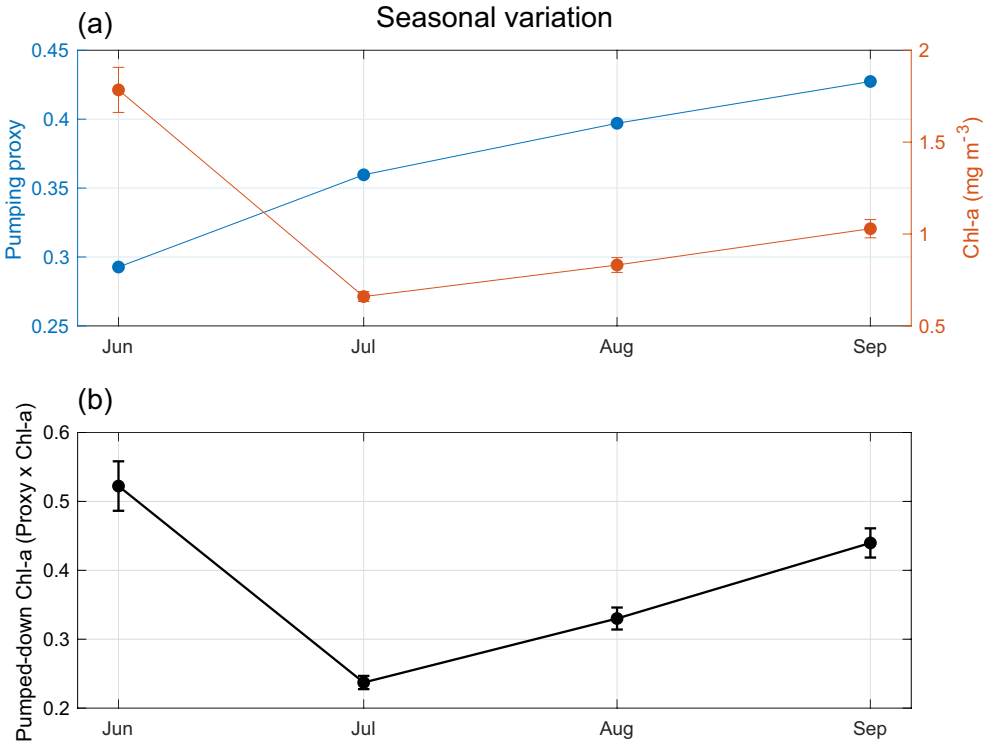

Figure 17. (a) Monthly mean values of the pumping proxy (blue) and source concentration of Chl *a* (red), for the period 2003–2018. (b) Carbon supply to the seafloor of Barrow Canyon (black), computed as the product of the two curves in (a). The standard errors for Chl *a* and the carbon supply are included.

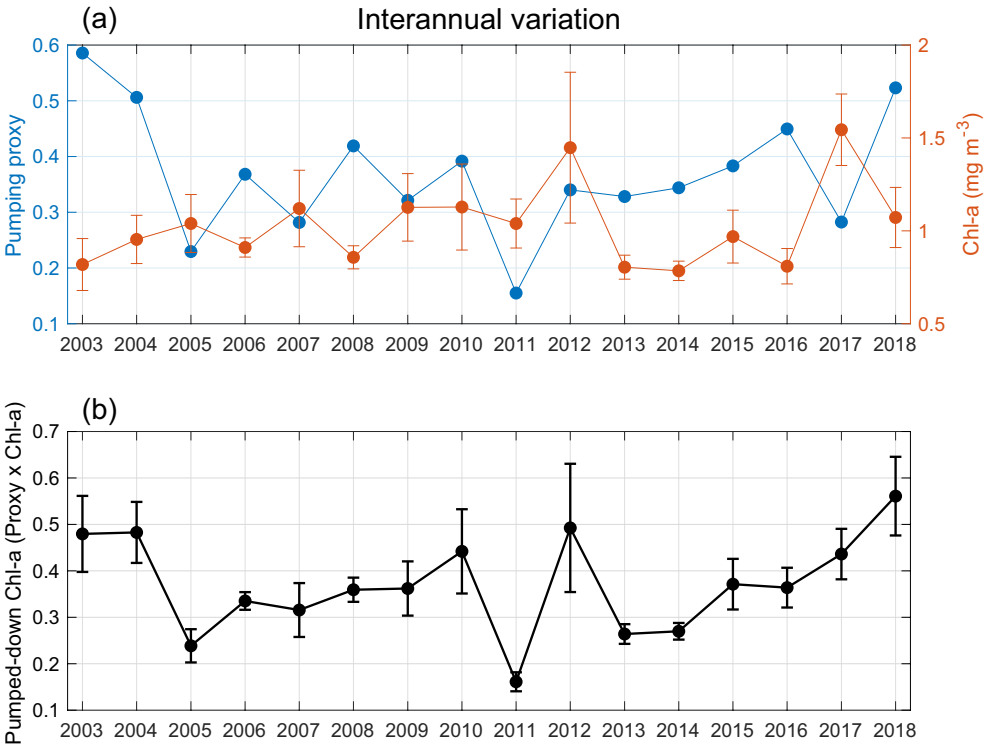

Figure 18. Same as Figure 17, except for the summertime (June to September) averages of the quantities for each year.

m wind record at Utqiaġvik, we computed the percentage of time over the three preceding days that winds out of the northeast exceeded 4 m s^{-1}. This revealed that all six pumping realizations had small values of this percentage (mean of 2.5%), in contrast to the nonpumping realizations (mean of 35.8%). Since all of the former were less than 6% and all of the latter were greater than this (see Table 1), we consider the ACC to be in a strong state when the percentage is less than 6%. The proxy is then defined as the percentage of time over a given month (for a seasonal comparison) or a given summer season (for an interannual comparison) that the ACC was in a strong state associated with vertical pumping.

Next, we seek to assess the magnitude of the carbon source, i.e., the amount of Chl *a* entering Barrow Canyon in the pycnocline (keep in mind that Chl *a* on the surface will not be pumped to the seafloor; see Figures 9b and 13d). Unfortunately, no time series of sub-surface Chl *a* in Barrow Canyon exist (and none of the cruises considered here measured Chl *a*). However, the blooms in question initiate on the surface of the Chukchi Sea and then migrate vertically to the pycnocline, as the nutrients are drawn down, prior to entering the canyon. It takes typically 1–3 weeks for this vertical displacement to occur (Brown et al., 2015; Martin et al., 2010; Palmer et al., 2011). Thus, if we know where on the shelf the water resided 1–3 weeks before reaching the canyon, we can use surface ocean color data to gauge the amount of phytoplankton available to be pumped down within the canyon.

Using the composite shipboard ADCP data set from Lin, Pickart, McRaven, et al. (2019), we computed back-trajectories from the DBO5 section onto the Chukchi shelf. In particular, we constructed a mean velocity map that excluded periods of strong northeasterly winds, which reverse the coastal flow, and also excluded periods when the wind stress curl over the interior shelf was positive, which disrupts the central shelf pathways (see Lin, Pickart, McRaven, et al., 2019). We then traced particles backwards in time using this mean velocity field to create a map of elapsed time to the canyon. This is shown in Figure 15, where we have highlighted the area corresponding to 1–3 weeks which is taken to be the source region. Accordingly, we constructed a time series of average Chl *a* within the source region using the MODIS satellite data. Figure 16 displays a MODIS image from June 2017 revealing significant bloom activity in the source region (This is shown as an example, and is not meant to imply that there is anything special about this region; indeed, bloom activity on the Chukchi shelf is patchy (Lewis et al., 2020; Lowry et al., 2015). The point is that there is plenty of Chl *a* present in the source region to supply Barrow Canyon).

At this point we have a proxy for the pumping and a time series of the Chl *a* entering the canyon, which can be multiplied together to represent the supply of carbon to the benthic fauna at the hotspot location. Considering the seasonal variation first, Figure 17a shows the monthly averaged pumping proxy and Chl *a* source for the warm months of the year (for the period 2003–2018, see Section 2). The pumping increases through the summer and peaks in September. By contrast, the Chl *a* is highest in June, associated with the open water bloom on the Chukchi shelf, with a slight increase in August and September reflecting a fall bloom. One sees that the resulting monthly carbon supply to the benthos is driven mainly by the Chl *a* source (Figure 17b).

Next, we address interannual variability. Computing the summertime (June to September, when the Chl *a* data are available) averages of the Chl *a* source and the pumping proxy, we find that they are statistically uncorrelated (Figure 18a). This is not surprising since there are many factors dictating the bloom activity on the northeast Chukchi shelf, including ice cover, wind mixing, and nutrient supply. By contrast, the proxy for pumping is determined by the local wind strength/direction in Barrow Canyon. When multiplying these time series together, it reveals that the variation in carbon supply is mainly dictated by the pumping rather than the Chl *a* source, opposite to the case of the seasonal variation (the carbon supply and pumping proxy time series are significantly correlated with $r = 0.72$, $p = 0.002$.) Hence, while pumping is necessary to flux the carbon to the hotspot—regardless of season—the variability in this physical control only has an imprint on the year-to-year variation in the food supply.

Unfortunately, it is difficult to relate this derived carbon supply to the seafloor to the macrofaunal benthic biomass data from the Barrow Canyon hotspot, for a number of reasons. First, the macrofaunal benthic communities (e.g., bivalves, polychaetes, sea anemones, basket stars, and tunicates) are long-lived and respond to the integrated food supply going back some period of time, likely a number of years. As such, their biomass will not change significantly due to shorter term variations in carbon supply, either month-to-

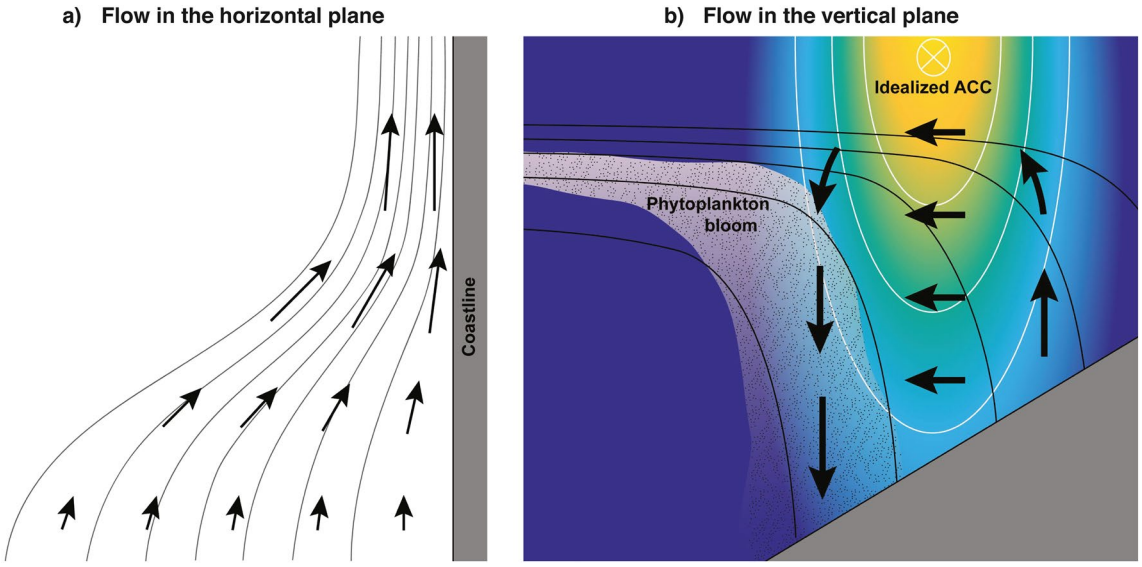

Figure 19. Schematic of the pumping process. (a) Convergence of the horizontal flow as it proceeds from upstream of the canyon to the center of the canyon. (b) Secondary circulation (vectors) showing the upwelling on the shoreward side of the density front (denoted by the thin contours) and the pumping on the seaward side of the density front. The ACC is flowing into the page (color and white contours). The phytoplankton plume is present on the cyclonic side of the ACC.

month variations (Figure 17) or averages over the entire summer (Figure 18). We integrated the estimated carbon supply (i.e., the pumping proxy multiplied by the Chl *a*) back in time over a range of 1–3 yr and compared this to the biomass data, but the results were not conclusive. This is perhaps not surprising since there are some gaps in the surface Chl *a* data which are exacerbated when integrating over a long period. There are also no satellite data for the month of October, which likely would have captured some early-fall bloom activity. Finally, there is significant scatter in the biomass data collected within a given season (or even within a given month) which could reflect spatial variability within the hotspot. Nonetheless, Figures 17 and 18 offer a view of the carbon supply on a seasonal and interannual basis which could be of use going forward, particularly if long-term trends start to emerge.

6. Conclusions

In this study, we have provided an explanation for why there is enhanced benthic macrofaunal biomass in the center of Barrow Canyon. It relies on a combination of the dynamics of the flow through the canyon along with the presence of a subsurface layer of phytoplankton in the pycnocline. Using a collection of 11 shipboard hydrographic/velocity crossings of the DBO5 transect in Barrow Canyon between 2009 and 2019, it was revealed that, in five instances, there was a sharp density front with near-vertically aligned isopycnals intersecting the bottom close to the deepest part of the canyon. The ACC was generally strong in these instances with a mean volume transport of >1 Sv. In four of the cases, plumes of high fluorescence and oxygen extended from the pycnocline to the seafloor in the vicinity of the benthic hotspot. The sole case without such vertical plumes was the only realization in which there was no subsurface chlorophyll maximum; instead, a surface bloom was present.

By contrast, three of the DBO crossings were characterized by a weak density front in which the isopycnals did not ground near the deepest part of the canyon (or in the canyon at all). In these cases the ACC was generally weaker, and there were no deep-reaching plumes of fluorescence and oxygen. As such, we classified the five sections with a strong ACC and strong density front as the pumping cases, and the three realizations with a generally weaker ACC and weaker density front as the non-pumping cases. Two of the remaining sections were occupied during upwelling conditions with strong up-canyon flow, and the final realization

was anomalous in that the ACC was located far inshore of its normal location. These three sections were excluded from the analysis.

By solving the quasi-geostrophic omega equation with an analytical flow field fashioned after the observed strong ACC cases, we diagnosed the vertical velocity in the canyon. This revealed that, as the along stream flow converges into the canyon, it drives a secondary circulation cell with strong downwelling on the cyclonic (offshore) side of the ACC, and weak upwelling on the anti-cyclonic (onshore) side of the ACC. The downwelling advects material from the pycnocline to the seafloor, forming a near-vertically aligned property plume analogous to the observed plumes of fluorescence and oxygen. This situation is shown schematically in Figure 19. The downwelling velocities are strong enough that the material reaches the bottom before the flow exits the canyon. However, if the tracer is introduced at the surface rather than in the pycnocline, no such deep-reaching plume is formed due to the weak vertical velocity in the upper portion of the water column. This is consistent with the observed case of a surface bloom in the canyon with no deep plume of fluorescence. A parameter space analysis of the omega equation revealed that, for large Rossby numbers, a significant fraction of the horizontal transport downwells in the center of Barrow Canyon. Based on the composite shipboard ADCP data set, Barrow Canyon is the only place along the path of the ACC where the Rossby number is large enough to cause strong pumping. This is not surprising because the canyon constricts the flow, resulting stronger velocity gradients there.

Making use of the relationship between wind forcing in the canyon and the strength of the ACC, we developed a proxy for the pumping that was applied to the long-term wind record from the weather station adjacent to the canyon. To assess the input of phytoplankton within the pycnocline of the canyon, we calculated back-trajectories from the DBO5 line to the Chukchi shelf using a mean velocity field based on climatological shipboard ADCP data. This was used to identify a source region where surface blooms would subsequently sink to the depth of the pycnocline by the time they reached the canyon. Using MODIS ocean color data, we then derived a source function of the phytoplankton. The product of this with the pumping proxy was taken to represent the carbon supply to the bottom of Barrow Canyon. This indicated that, seasonally, the carbon supply is mainly dictated by the Chl *a* source, whereas changes in pumping have a dominant influence on interannual time scales. Our results thus reveal a coupled bio-physical mechanism that explains the existence of the benthic hotspot in Barrow Canyon, which is largely dictated by the dynamics of the strong northward flow through the canyon. It also suggests that the predicted increased storminess in a warming climate, with stronger northeasterly winds, could significantly modulate this signal.

Data Availability Statement

The CTD data used in the study are available at https://arcticdata.io. The benthic macrofaunal data are available through the Arctic Data Center (J. M. Grebmeier & Cooper, 2020) at https://arcticdata.io/catalog/portals/DBO/Data.

Acknowledgments
The authors are indebted to the many officers and crew members of USCGC *Healy* who enabled the collection of the DBO5 measurements, and to the individuals who processed the shipboard hydrographic data. This work was funded by National Science Foundation grants PLR-1504333 and OPP-1733564 (Robert S. Pickart, Frank Bahr), OPP-1822334 (Michael A. Spall), PLR-1304563 (Kevin R. Arrigo), OPP-1204082 and OPP-1702456 (Jacqueline M. Grebmeier); National Oceanic and Atmospheric Administration grants NA14OAR4320158 and NA19OAR4320074 (Robert S. Pickart, Peigen Lin, Leah T. McRaven), CINAR-22309.02 (Jacqueline M. Grebmeier).

References

Arrigo, K. R., Mills, M. M., van Dijken, G. L., Lowry, K. E., Pickart, R. S., & Schlitzer, R. (2017). Late spring nitrate distributions beneath the ice-covered northeastern Chukchi shelf. *Journal of Geophysical Research: Biogeosciences*, *122*(9), 2409–2417. https://doi.org/10.1002/2017jg003881

Arrigo, K. R., & van Dijken, G. L. (2011). Secular trends in Arctic Ocean net primary production. *Journal of Geophysical Research: Oceans*, *116*(C9). https://doi.org/10.1029/2011jc007151

Bannon, C. C., & Campbell, D. A. (2017). Sinking toward destiny: High throughput measurement of phytoplankton sinking rates through time-resolved fluorescence plate spectroscopy. *PLoS One*, *12*(10), e0185166. https://doi.org/10.1371/journal.pone.0185166

Beaird, N., Shroyer, E., Juranek, L., Hales, B., & Goñi, M. (2020). Nutrient-rich gravity current formed by upwelling in barrow canyon: High-resolution observations. *Journal of Geophysical Research: Oceans*, *125*(7), e2020JC016160. https://doi.org/10.1029/2020jc016160

Blumsack, S. L., & Gierasch, P. J. (1972). Mars: The effects of topography on baroclinic instability. *Journal of the Atmospheric Sciences*, *29*(6), 1081–1089. https://doi.org/10.1175/1520-0469(1972)029<1081:mteoto>2.0.co;2

Brearley, J. A., Pickart, R. S., Valdimarsson, H., Jonsson, S., Schmitt, R. W., & Haine, T. W. N. (2012). The East Greenland boundary current system south of Denmark Strait. *Deep Sea Research Part I: Oceanographic Research Papers*, *63*, 1–19. https://doi.org/10.1016/j.dsr.2012.01.001

Brown, Z. W., Lowry, K. E., Palmer, M. A., van Dijken, G. L., Mills, M. M., Pickart, R. S., & Arrigo, K. R. (2015). Characterizing the subsurface chlorophyll *a* maximum in the Chukchi Sea and Canada Basin. *Deep Sea Research Part II: Topical Studies in Oceanography*, *118*, 88–104. https://doi.org/10.1016/j.dsr2.2015.02.010

Coachman, L. (1967). *Oceanography, Naval Arctic Manual ATP-17 (A). Part I: Environment* (Vol. 3, pp. 1–18). Montreal: Arctic Institute of North America.

Corlett, W. B., & Pickart, R. S. (2017). The Chukchi slope current. *Progress in Oceanography*, *153*, 50–65. https://doi.org/10.1016/j.pocean.2017.04.005

Eppley, R. W., Holmes, R. W., & Strickland, J. D. H. (1967). Sinking rates of marine phytoplankton measured with a fluorometer. *Journal of Experimental Marine Biology and Ecology*, *1*(2), 191–208. https://doi.org/10.1016/0022-0981(67)90014-7

Fang, Y. C., Weingartner, T. J., Dobbins, E. L., Winsor, P., Statscewich, H., Potter, R. A., et al. (2020). Circulation and thermohaline variability of the hanna shoal region on the northeastern chukchi sea shelf. *Journal of Geophysical Research: Oceans*, *125*(7), p.e2019JC015639.

Feng, Z., Ji, R., Ashjian, C., Zhang, J., Campbell, R., & Grebmeier, J. M. (2021191). Benthic hotspots on the northern Bering and Chukchi Continental shelf: Spatial variability in production regimes and environmental drivers. *Progress in Oceanography*, *191*, 102497. https://doi.org/10.1016/j.pocean.2020.102497

Gong, D., & Pickart, R. S. (2015). Summertime circulation in the eastern Chukchi Sea. *Deep Sea Research Part II: Topical Studies in Oceanography*, *118*, 18–31. https://doi.org/10.1016/j.dsr2.2015.02.006

Gong, D., & Pickart, R. S. (2016). Early summer water mass transformation in the eastern Chukchi Sea. *Deep Sea Research Part II: Topical Studies in Oceanography*, *130*, 43–55. https://doi.org/10.1016/j.dsr2.2016.04.015

Grebmeier, J. M., Bluhm, B. A., Cooper, L. W., Danielson, S. L., Arrigo, K. R., Blanchard, A. L., et al. (2015). Ecosystem characteristics and processes facilitating persistent macrobenthic biomass hotspots and associated benthivory in the Pacific Arctic. *Progress in Oceanography*, *136*, 92–114. https://doi.org/10.1016/j.pocean.2015.05.006

Grebmeier, J. M., & Cooper, L. W. (2020). *Benthic macrofaunal and dominant taxa samples collected from Northern Bering Sea to Chukchi Sea. 1970–2017*. Arctic Data Center. https://doi.org/10.18739/A2SX6499X

Grebmeier, J. M., Cooper, L. W., Feder, H. M., & Sirenko, B. I. (2006). Ecosystem dynamics of the Pacific-influenced northern Bering and Chukchi seas in the Amerasian Arctic. *Progress in Oceanography*, *71*, 331–361. https://doi.org/10.1016/j.pocean.2006.10.001

Grebmeier, J. M., Frey, K. E., Cooper, L. W., & Kędra, M. (2018). Trends in benthic macrofaunal populations, seasonal sea ice persistence, and bottom water temperatures in the Bering Strait region. *Oceanography*, *31*(2), 136–151. https://doi.org/10.5670/oceanog.2018.224

Hoskins, B. J., Draghici, I., & Davies, H. C. (1978). A new look at the ω-equation. *Quarterly Journal of the Royal Meteorological Society*, *104*(439), 31–38. https://doi.org/10.1002/qj.49710443903

Itoh, M., Nishino, S., Kawaguchi, Y., & Kikuchi, T. (2013). Barrow Canyon volume, heat, and freshwater fluxes revealed by long-term mooring observations between 2000 and 2008. *Journal of Geophysical Research: Oceans*, *118*(9), 4363–4379. https://doi.org/10.1002/jgrc.20290

Itoh, M., Pickart, R. S., Kikuchi, T., Fukamachi, Y., Ohshima, K. I., Simizu, D., et al. (2015). Water properties, heat, and volume fluxes of Pacific water in Barrow Canyon during summer 2010. *Deep Sea Research Part I: Oceanographic Research Papers*, *102*, 43–54. https://doi.org/10.1016/j.dsr.2015.04.004

Ladd, C., Mordy, C. W., Salo, S. A., & Stabeno, P. J. (2016). Winter water properties and the Chukchi Polynya. *Journal of Geophysical Research: Oceans*, *121*(8), 5516–5534. https://doi.org/10.1002/2016jc011918

Lentz, S. J., & Winant, C. D. (1986). Subinertial currents on the southern Califoinia shelf. *Journal of Physical Oceanography*, *16*(11), 1737–1750. https://doi.org/10.1175/1520-0485(1986)016<1737:scotsc>2.0.co;2

Lewis, K. M., van Dijken, G. L., & Arrigo, K. R. (2020). Changes in phytoplankton concentration now drive increased Arctic Ocean primary production. *Science*, *369*, 198–202. https://doi.org/10.1126/science.aay8380

Lin, P., Pickart, R. S., Jochumsen, K., Moore, G. W. K., Valdimarsson, H., Fristedt, T., & Pratt, L. J. (2020). Kinematic structure and dynamics of the Denmark Strait overflow from ship-based observations. *Journal of Physical Oceanography*, *50*(11), 3235–3251. https://doi.org/10.1175/jpo-d-20-0095.1

Lin, P., Pickart, R. S., McRaven, L. T., Arrigo, K. R., Bahr, F., Lowry, K. E., et al. (2019). Water mass evolution and circulation of the northeastern Chukchi Sea in summer: Implications for nutrient distributions. *Journal of Geophysical Research: Oceans*.

Lowry, K. E., Pickart, R. S., Mills, M. M., Brown, Z. W., van Dijken, G. L., Bates, N. R., & Arrigo, K. R. (2015). The influence of winter water on phytoplankton blooms in the Chukchi Sea. *Deep Sea Research Part II: Topical Studies in Oceanography*, *118*, 53–72. https://doi.org/10.1016/j.dsr2.2015.06.006

MacKinnon, J., Simmons, H. L., Hargrove, J. T., Thomson, J., Peacock, T., Alford, M. H., et al. (2020). Subduction of Pacific summer water into sub-surface eddies; coordinated observations from late summer 2018. *Eos Transaction AGU*, abstract, HE43A-04.

Martin, J., Tremblay, J., Gagnon, J., Tremblay, G., Lapoussière, A., Jose, C., et al. (2010). Prevalence, structure and properties of subsurface chlorophyll maxima in Canadian Arctic waters. *Marine Ecology Progress Series*, *412*, 69–84. https://doi.org/10.3354/meps08666

Moore, S. E., Grebmeier, J. M., & Giguère, N. (2018). The Distributed Biological Observatory. *Arctic*, *71*, 1–7. https://doi.org/10.14430/arctic4606

Pacini, A., Moore, G. W. K., Pickart, R. S., Nobre, C., Bahr, F., Våge, K., & Arrigo, K. R. (2019). Characteristics and transformation of Pacific winter water on the Chukchi Sea shelf in late spring. *Journal of Geophysical Research: Oceans*, *124*(10), 7153–7177. https://doi.org/10.1029/2019jc015261

Padman, L., & Erofeeva, S. (2004). A barotropic inverse tidal model for the Arctic Ocean. *Geophysical Research Letters*, *31*(2). https://doi.org/10.1029/2003gl019003

Palmer, M. A., Arrigo, K. R., Mundy, C. J., Ehn, J. K., Gosselin, M., Barber, D. G., et al. (2011). Spatial and temporal variation of photosynthetic parameters in natural phytoplankton assemblages in the Beaufort Sea, Canadian Arctic. *Polar Biology*, *34*, 1915–1928. https://doi.org/10.1007/s00300-011-1050-x

Paquette, R. G., & Bourke, R. H. (1974). Observations on the coastal current of Arctic Alaska. *Journal of Marine Research*, *32*, 195–207.

Pedlosky, J. (1979). Finite-amplitude baroclinic waves in a continuous model of the atmosphere. *Journal of the Atmospheric Sciences*, *36*(10), 1908–1924. https://doi.org/10.1175/1520-0469(1979)036<1908:fabwia>2.0.co;2

Pickart, R. S., Moore, G. W. K., Mao, C., Bahr, F., Nobre, C., & Weingartner, T. J. (2016). Circulation of winter water on the Chukchi shelf in early summer. *Deep Sea Research Part II: Topical Studies in Oceanography*, *130*, 56–75. https://doi.org/10.1016/j.dsr2.2016.05.001

Pickart, R. S., Nobre, C., Lin, P., Arrigo, K. R., Ashjian, C. J., Berchok, C., et al. (2019). Seasonal to mesoscale variability of water masses and atmospheric conditions in Barrow Canyon, Chukchi Sea. *Deep Sea Research Part II: Topical Studies in Oceanography*, *162*, 32. https://doi.org/10.1016/j.dsr2.2019.02.003

Pickart, R. S., Pratt, L. J., Torres, D. J., Whitledge, T. E., Proshutinsky, A. Y., Aagaard, K., et al. (2010). Evolution and dynamics of the flow through Herald Canyon in the western Chukchi Sea. *Deep Sea Research Part II: Topical Studies in Oceanography*, *57*(1–2), 5–26. https://doi.org/10.1016/j.dsr2.2009.08.002

Pickart, R. S., Schulze, L. M., Moore, G. W. K., Charette, M. A., Arrigo, K. R., van Dijken, G., & Danielson, S. L. (2013). Long-term trends of upwelling and impacts on primary productivity in the Beaufort Sea. *Deep-Sea Research I*, *79*, 106–121.

Pickart, R. S., & Stossmeister, G. (2008). Outflow of Pacific water from the Chukchi Sea to the Arctic Ocean. *Chinese Journal of Polar Oceanography*, *19*(2-English), 135–148.

Pickart, R. S., Torres, D. J., & Fratantoni, P. S. (2005). The East Greenland Spill Jet*. *Journal of Physical Oceanography*, *35*(6), 1037–1053. https://doi.org/10.1175/jpo2734.1

Pisareva, M. N., Pickart, R. S., Lin, P., Fratantoni, P. S., & Weingartner, T. J. (2019). On the nature of wind-forced upwelling in Barrow Canyon. *Deep Sea Research Part II: Topical Studies in Oceanography*, *162*, 63. https://doi.org/10.1016/j.dsr2.2019.02.002

Pisareva, M. N., Pickart, R. S., Spall, M. A., Nobre, C., Torres, D. J., Moore, G. W. K., & Whitledge, T. E. (2015). Flow of Pacific water in the western Chukchi Sea: Results from the 2009 RUSALCA expedition. *Deep Sea Research Part I: Oceanographic Research Papers*, *105*, 53–73. https://doi.org/10.1016/j.dsr.2015.08.011

Schulze, L. M., & Pickart, R. S. (2012). Seasonal variation of upwelling in the Alaskan Beaufort Sea: Impact of sea ice cover. *Journal of Geophysical Research*, *117*(C06022). https://doi.org/10.1029/2012jc007985

Shroyer, E. L. (2012). Turbulent kinetic energy dissipation in Barrow Canyon. *Journal of Physical Oceanography*, *42*(6), 1012–1021. https://doi.org/10.1175/jpo-d-11-0184.1

Spall, M. A., & Pedlosky, J. (2008). Lateral coupling in baroclinically unstable flows. *Journal of Physical Oceanography*, *38*(6), 1267–1277. https://doi.org/10.1175/2007jpo3906.1

Springer, A. M., & McRoy, C. P. (1993). The paradox of pelagic food webs in the northern Bering Sea—III. Patterns of primary production. *Continental Shelf Research*, *13*(5–6), 575–599. https://doi.org/10.1016/0278-4343(93)90095-f

Weingartner, T., Aagaard, K., Woodgate, R., Danielson, S., Sasaki, Y., & Cavalieri, D. (2005). Circulation on the north central Chukchi Sea shelf. *Deep Sea Research Part II: Topical Studies in Oceanography*, *52*(24), 3150–3174. https://doi.org/10.1016/j.dsr2.2005.10.015

Weingartner, T. J., Potter, R. A., Stoudt, C. A., Dobbins, E. L., Statscewich, H., Winsor, P. R., et al. (2017). Transport and thermohaline variability in Barrow Canyon on the northeastern Chukchi Sea shelf. *Journal of Geophysical Research: Oceans*, *122*(5), 3565–3585. https://doi.org/10.1002/2016jc012636

Woodgate, R. A. (2018). Increases in the Pacific inflow to the Arctic from 1990 to 2015, and insights into seasonal trends and driving mechanisms from year-round Bering Strait mooring data. *Progress in Oceanography*, *160*, 124–154. https://doi.org/10.1016/j.pocean.2017.12.007